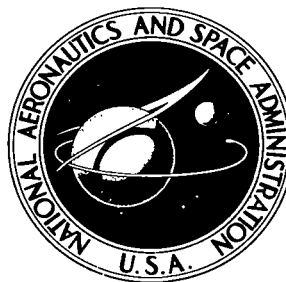


NASA TECHNICAL NOTE



NASA TN D-6885

c. 1

NASA TN D-6885

LOAN COPY: RETURN
AFWL (DOUL)
KIRTLAND AFB, N. M.



**NUMERICAL SOLUTIONS OF SEVERAL
REFLECTED SHOCK-WAVE FLOW FIELDS
WITH NONEQUILIBRIUM CHEMICAL REACTIONS**

*by Ronald K. Hanson, Leroy L. Presley,
and Elsie V. Williams*

*Ames Research Center
Moffett Field, Calif. 94035*



0133640

1. Report No. NASA TN D-6885	2. Government Accession No.	3. Recipient's Catalog No.	
4. Title and Subtitle NUMERICAL SOLUTIONS OF SEVERAL REFLECTED SHOCK-WAVE FLOW FIELDS WITH NONEQUILIBRIUM CHEMICAL REACTIONS		5. Report Date August 1972	
		6. Performing Organization Code	
7. Author(s) Ronald K. Hanson (NRC-NASA postdoctoral fellow), Leroy L. Presley, and Elsie V. Williams		8. Performing Organization Report No. A-4226	
		10. Work Unit No. 117-07-04-13-00-21	
9. Performing Organization Name and Address NASA Ames Research Center Moffett Field, Calif. 94035		11. Contract or Grant No.	
		13. Type of Report and Period Covered Technical Note	
12. Sponsoring Agency Name and Address National Aeronautics and Space Administration Washington, D.C. 20546		14. Sponsoring Agency Code	
		15. Supplementary Notes	
16. Abstract <p>The method of characteristics for a chemically reacting gas is used in the construction of the time-dependent, one-dimensional flow field resulting from the normal reflection of an incident shock wave at the end wall of a shock tube. Nonequilibrium chemical reactions are allowed behind both the incident and reflected shock waves. All the solutions are evaluated for oxygen, but the results are generally representative of any inviscid, nonconducting, and nonradiating diatomic gas. The solutions clearly show that (1) both the incident- and reflected-shock chemical-relaxation times are important in governing the time to attain steady-state thermodynamic properties; and (2) adjacent to the end wall, an excess-entropy layer develops wherein the steady-state values of all the thermodynamic variables except pressure differ significantly from their corresponding Rankine-Hugoniot equilibrium values.</p>			
17. Key Words (Suggested by Author(s)) Shock wave Method of characteristics Nonequilibrium Oxygen		18. Distribution Statement Unclassified - Unlimited	
19. Security Classif. (of this report) Unclassified	20. Security Classif. (of this page) Unclassified	21. No. of Pages 49	22. Price* \$3.00



SYMBOLS

A	mass-flux constant, equation (1)
a	sound speed at fixed composition, cm/sec
B	momentum-flux constant, equation (2)
C	total enthalpy constant, equation (3)
c_{pf}	constant-pressure specific heat at frozen composition, cal/initial mole-°K
D	dissociation energy (117,960 cal/mole for O ₂); also, total derivative
G	nonequilibrium characteristics term, equation (25), g/cm ³ -sec
h	static enthalpy per initial mole of molecules, cal/mole
K_c	equilibrium constant, moles/cm ³
k_d	dissociation rate, cm ³ /mole-sec
k_r	recombination rate, cm ⁶ /mole ² -sec
O	oxygen atom
O_2	oxygen molecule
P	pressure, atm, or dynes/cm ²
p	partial pressure, atm
R	universal gas constant, 1.987 cal/mole-°K, or 82.06 cm ³ -atm/mole-°K
R'	specific gas constant, 2.598×10 ⁶ ergs/g-°K for O ₂
S	entropy per unit mass, cal/g-°K
T	temperature, °K
t	time, sec
U	velocity of incident shock wave relative to end wall, cm/sec
u	velocity of gas behind reflected shock wave relative to end wall, cm/sec
V	velocity of reflected shock wave relative to end wall, cm/sec

v	velocity of gas behind incident shock wave relative to incident shock, cm/sec
W	molecular weight of diatomic gas (32 g/mole for O_2)
w	mass rate of production of a chemical species, g/cm^3 -sec
x	distance from shock-tube end wall, cm
α	degree of dissociation (equals, ρ_0/ρ)
β	arbitrary multiplier of recombination rate
δ	derivative along characteristic line
θ_d	characteristic temperature of dissociation ($58,960^\circ$ K for O_2)
θ_v	characteristic temperature of vibration ($2,274^\circ$ K for O_2)
μ	chemical potential, cal/g
ρ	mass density, g/cm^3
τ	characteristic time
[]	concentration, moles/ cm^3

Subscripts

eq	equilibrium
k	specific chemical species
1	ahead of incident shock wave
2	behind incident shock wave
3	behind reflected shock wave
30	behind reflected shock wave at instant of reflection
2 <i>i</i>	general spatial point behind incident shock wave

**NUMERICAL SOLUTIONS OF SEVERAL REFLECTED SHOCK-WAVE
FLOW FIELDS WITH NONEQUILIBRIUM
CHEMICAL REACTIONS**

Ronald K. Hanson,* Leroy L. Presley, and Elsie V. Williams

Ames Research Center

SUMMARY

The method of characteristics for a chemically reacting gas is used in the construction of the time-dependent, one-dimensional flow field resulting from the normal reflection of an incident shock wave at the end wall of a shock tube. Nonequilibrium chemical reactions are allowed behind both the incident and reflected shock waves. All the solutions are evaluated for oxygen, but the results are generally representative of any inviscid, nonconducting, and nonradiating diatomic gas. The solutions clearly show that (1) both the incident- and reflected-shock chemical-relaxation times are important in governing the time to attain steady-state thermodynamic properties; and (2) adjacent to the end wall, an excess-entropy layer develops wherein the steady-state values of all the thermodynamic variables except pressure differ significantly from their corresponding Rankine-Hugoniot equilibrium values.

INTRODUCTION

The use of shock tubes for studies of high-temperature gasdynamics and nonequilibrium chemical kinetics is well established. Many of these studies consisted of observations of the gas heated by the reflection of an incident or primary shock wave at the end wall of a shock tube (Johnson and Britton, ref. 1). Reflected-shock testing has two major advantages: First, the temperature behind the reflected shock wave is increased to roughly twice that behind the incident shock wave. Second, the gas behind the reflected shock wave is nearly stationary in laboratory coordinates; thus greater time resolution can be achieved for studying nonequilibrium processes, for example, than is obtainable behind shock waves at the same thermodynamic conditions.

However, several phenomena occur behind a reflected shock wave that can limit its usefulness in producing a well-defined sample of hot test gas. For the most part, these phenomena give rise to uncertainties in the thermodynamic state of the test gas. Three phenomena occur as a consequence of the side-wall viscous boundary layer that develops behind the incident shock wave. First, the presence of the boundary layer induces spatially nonuniform properties within the core of the flow field behind the incident shock wave, thus causing time-dependent upstream properties for

*NRC-NASA postdoctoral fellow.

the reflected shock wave. From their analyses of this problem, Kamimoto et al. (ref. 2) and Rudinger (ref. 3) have concluded that the nonuniform flow is responsible for the slow pressure rise often observed on the end wall of a shock tube after shock reflection. The second phenomenon is the initiation of a complicated shock-wave-boundary-layer interaction as the reflected shock propagates back through the side-wall boundary layer. This interaction is more intense in gases of greater molecular complexity. Mark (ref. 4) and Strehlow and Cohen (ref. 5) have observed the bifurcation resulting from the interaction and concluded that the effect is negligible for monatomic gases and is sufficiently small for diatomic gases to permit kinetics studies immediately adjacent to the end wall. In an interferometric study of strong shocks in dissociating nitrogen, Hanson (unpublished results (1968)) observed increasing bifurcation with increasing shock speed and decreasing test pressure, and found that the flow near the end wall remained suitable for kinetics studies only for the short times prior to serious bifurcation effects. Third, the side-wall boundary layer causes the incident shock wave to be curved. On the basis of experimental data, Lin and Fyfe (ref. 6) argued that the center displacement of the incident shock wave is directly proportional to $(r/\rho_1)^{1/2}$, where r is the shock-tube radius and ρ_1 is the initial density. The effects of a curved incident shock wave on a reflected-shock-wave flow field, however, are not well understood.

A fourth phenomenon that complicates the reflected-shock-wave flow field arises from the thermal boundary layer that forms on the end wall of the shock tube. Sturtevant and Slachmuylders (ref. 7) have studied, both theoretically and experimentally, the effect of the end-wall thermal boundary layer on the trajectory of the reflected shock wave; and Goldsworthy (ref. 8) has obtained expressions for the flow-field perturbations resulting from the boundary-layer formation. Generally, these results show that if the initial tube pressure is greater than about 1 torr, the effects of the heat transfer on the flow field are not significant at distances greater than 1 mm from the end wall, provided observation times are less than a few hundred microseconds.

Since all the aforementioned phenomena result from viscous or heat-conduction effects, the controlling factors, if not the phenomena themselves, are well understood. These complications can thus be minimized by appropriate selection of experimental technique, test conditions, and observation interval. However, an additional problem exists for studies involving nonequilibrium chemical reactions because an adequate theory for predicting the entire nonequilibrium flow field in even an inviscid and nonconducting gas has not been available. This latter aspect of shock-wave reflection is the subject to which this paper is addressed. A simple model for shock-wave reflection in a relaxing gas has been presented by Hanson (ref. 9), but results based on that model apply only to the layer of gas immediately adjacent to the end wall. The problem here is to determine the entire reflected-shock flow field when nonequilibrium chemical reactions are present behind both the incident and reflected shock waves. The method of characteristics for a one-dimensional reacting gas is used in obtaining numerical solutions.

The closely related problem of reflected-shock flow fields with vibrational nonequilibrium was first discussed qualitatively by Baganoff (ref. 10) with particular emphasis on the vibrational relaxation of carbon dioxide. More recently, Johannesen et al. (ref. 11) have obtained quantitative results for the vibrational relaxation of carbon dioxide behind reflected shock waves by means of the method of characteristics. Many of the general features of these works also appear in the present results, although the emphasis of this work is on defining quantitatively the effect of nonequilibrium *chemical reactions* on a reflected-shock flow field. A simple chemical model has been used to show clearly the coupling between the fluid mechanics and chemistry. Once the basic features of a

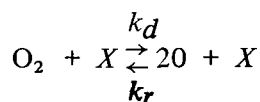
nonequilibrium reflected-shock flow field are understood, a more complicated chemical model can readily be implemented.

METHOD OF ANALYSIS

The problem of finding a solution for a reflected-shock flow field with nonequilibrium chemical reactions introduces several phenomena that are not considered in the usual equilibrium solutions of reflected-shock properties. For example, nonequilibrium flow behind the incident shock wave causes curvature of the particle paths in the xt plane (see fig. 1), and results in a spatial gradient in all the fluid and thermodynamic properties behind the incident shock wave. The reflected shock wave must propagate back into this nonuniform region; hence the properties upstream of the reflected shock are continually changing. As a result of both the time-varying upstream properties and the nonequilibrium chemical reactions occurring behind the reflected shock wave, the velocity of the reflected shock wave is not constant (fig. 1). In addition, the usual boundary condition of zero flow velocity behind the reflected shock applied for an ideal gas now holds only at the end wall, and the particle paths behind the reflected shock wave are curved. These factors complicate the flow-field calculations by preventing selection of a coordinate system in which the flow across the reflected shock wave appears steady, as is possible with incident-shock-wave calculations.

Since the relaxation region behind the incident shock wave is independent of the reflected shock wave, it is possible to separate the overall solution for shock reflection into two portions: (1) flow behind the incident shock wave, and (2) flow behind the reflected shock wave. Several assumptions regarding the mathematical model used to obtain solutions are:

1. The gas is a mixture of thermally perfect gases.
2. The vibrational energy is in equilibrium at the local translational temperature and is given by a nontruncated harmonic-oscillator model.
3. All molecules and atoms remain in their ground electronic states.
4. The reaction under study is the dissociation of molecular oxygen,



where X denotes an arbitrary collision partner that may be either molecular or atomic oxygen.

5. The ratio of the dissociation and recombination rate constants is the equilibrium constant evaluated at the local translational temperature.
6. The flow is one-dimensional in a constant-area tube.
7. All transport processes are neglected.
8. The end wall is chemically inert.

These assumptions greatly simplify the study without changing the principal features of the coupling between nonequilibrium chemical reactions and fluid mechanics in a reflected-shock flow field.

Incident-Shock Solution

The solution of incident-shock-wave flow fields with finite-rate chemistry is straightforward (ref. 12), primarily because the flow is steady in a shock-fixed coordinate system. The set of equations describing the steady, one-dimensional flow of a dissociating diatomic gas behind a normal shock wave are as follows; in shock-fixed coordinates:

Conservation equations.

Mass:

$$\rho_1 U = (\rho v)_{2i} = A \quad (1)$$

Momentum:

$$P_1 + \rho_1 U^2 = P_{2i} + (\rho v^2)_{2i} = B \quad (2)$$

Energy:

$$h_1 + (1/2)U^2 = h_{2i} + (1/2)v_{2i}^2 = C \quad (3)$$

Equations of state.

Thermal:

$$P = (1 + \alpha) \frac{R}{W} \rho T \quad (4)$$

or

$$P = (1 + \alpha) R' \rho T \quad (5)$$

Caloric:

$$h = \left(\frac{7 + 3\alpha}{2} \right) RT + \frac{(1 - \alpha) R \theta_v}{e^{\theta_v/T} - 1} + \alpha D \quad (6)$$

Rate equation.

$$\frac{D\alpha}{Dt} = \frac{W}{\rho} (k_d [\text{O}_2] [X] - k_r [\text{O}]^2 [X]) \quad (7)$$

where

$$k_r = \beta A T^m \quad (8)$$

$$k_d = K_C k_r \quad (9)$$

$$K_C = 0.666 T^{1/2} e^{-\theta_d/T} \left(1 - e^{-\theta_v/T} \right) \quad (10)$$

The total molar concentration $[X]$ is simply

$$[X] = \frac{P}{RT} \quad (11)$$

while the molecular molar concentration is

$$[O_2] = \frac{1 - \alpha}{1 + \alpha} [X] \quad (12)$$

and the atomic molar concentration is

$$[O] = \frac{2\alpha}{1 + \alpha} [X] \quad (13)$$

The quantities A , B , and C are constants for each flow case, readily evaluated for specified initial conditions and shock speed. The rate constant k_r actually used in the numerical calculations was chosen subjectively on the basis of several experimental studies (see, e.g., Green and Toennies, ref. 13). The values of A and m selected are 7.29×10^{21} ($\text{cm}^6/\text{mole}^2\text{-sec}$) and -2 , respectively; β is a multiplier for conveniently varying the magnitude of the rate constant. The simplified expression for the equilibrium constant K_C is given in appendix A. Equations (4) through (13) also apply to the flow behind a reflected shock wave.

The above set of equations is solved at each point $2i$ ($i = 0, 1, 2, \dots$) in the incident-shock flow field, subject to the following boundary conditions: (1) no dissociation occurs across the shock front, that is, the chemistry is frozen¹ at $\alpha = 0$; and (2) equilibrium is reached when $D\alpha/Dt$ goes to zero. The procedure makes use of two independent equations for the gas velocity v_{2i} obtained from equations (1), (2), (3), and (5):

$$v_{2i} = \frac{B}{2A} - \left(\frac{1}{2} \right) \left[\left(\frac{B}{A} \right)^2 - 4R'T_{2i}(1 + \alpha_{2i}) \right]^{1/2} \quad (14)$$

and

$$v_{2i} = [2(C - h_{2i})]^{1/2} \quad (15)$$

Immediately behind the shock, at point 2_0 , the value of α is zero, and T_{2_0} may be found by varying the temperature until the same value of v_{2_0} is obtained in equations (14) and (15). Subsequent flow-field points are fixed by selecting the value of T_{2i} according to

$$T_{2i} = T_{2_0} - i\Delta T \quad (16)$$

¹In this paper, "frozen" chemistry refers to fixed composition (fixed α).

where ΔT is a computer input quantity usually taken to be 100° K. The variable α_{2i} is found by simple iteration using equations (14) and (15) with the known value of T_{2i} . It is clear that for any given shock wave, once a single thermodynamic quantity is known, at any flow-field point, all the remaining variables can be found directly.

The position of each flow-field point is still unknown, however, and must be found by numerical integration of the rate equation. The increment of length between adjacent flow-field points is given by

$$(\Delta x)_{2i} = \frac{\alpha_{2i} - \alpha_{2(i-1)}}{(d\alpha/dx)_{av}} \quad (17)$$

where

$$\left(\frac{d\alpha}{dx}\right)_{av} = \frac{1}{2} \left[\left(\frac{d\alpha}{dx}\right)_{2(i-1)} + \left(\frac{d\alpha}{dx}\right)_{2i} \right] \quad (18)$$

and the values of $d\alpha/dx$ are computed from equation (7). (Note: $D\alpha/DT = v_{2i}(d\alpha/dx)_{2i}$ for the steady flow behind the incident shock wave.) The total distance of point $2i$ from the incident shock front is

$$x_{2i} = \sum_{j=1}^i (\Delta x)_{2j} \quad (19)$$

In practice, calculations continue so long as $d\alpha/dx$ is positive; when $d\alpha/dx$ goes negative, equilibrium has been passed, and the program goes back at least two flow-field stations and computes forward with smaller temperature steps (generally 10° K) until equilibrium is again passed. The program then backs up again and computes forward with a final, yet smaller temperature-step size (generally 2° K). This small-step portion of the program is necessary to minimize errors in computed relaxation length near equilibrium.

The actual equilibrium conditions can be established independently of the rate equation, of course, from equations (1) through (6) and the law of mass action,

$$K_c = \frac{4\alpha^2}{1 - \alpha^2} [X] = \frac{4\alpha^2}{1 - \alpha} \frac{\rho}{W} \quad (20)$$

For a homonuclear diatomic gas, the appropriate equations to solve are:

$$A^2 = \left(\frac{1-\alpha}{\alpha^2}\right) K_c B \frac{W}{4} - \left\{ \frac{1-\alpha}{\alpha^2} \frac{W}{4} K_c \right\}^2 R' T (1 + \alpha) \quad (21)$$

and

$$A^2 = 2 \left\{ \left(\frac{1-\alpha}{\alpha^2}\right) \frac{W}{4} K_c \right\}^2 (C - h) \quad (22)$$

The equilibrium constant K_c is a function of T alone (eq. (10)) and h is a function of T and α , so that simultaneous solution of equations (21) and (22) yields the equilibrium values of T and α behind the incident shock wave. Other equilibrium property values follow from the conservation and state relations.

Flow-field properties throughout the incident-shock nonequilibrium zone are stored in computer memory since they provide the time-varying upstream conditions for the reflected shock wave.

Reflected-Shock Solution

The entire flow field behind the reflected shock wave is constructed using the method of characteristics. A derivation of the appropriate characteristic equations is given in appendix B (see also Ferri (ref. 14) and Chu (ref. 15)); only the final form of the equations is used here. In addition, since the complete calculation procedure is very lengthy, only a brief description of the logic of the numerical solution is presented here; a more detailed discussion is provided in appendixes C, D, and E.

Basic equations—The equations of motion for a reacting gas, as for a nonreacting gas, can be simplified to ordinary differential form along the characteristic directions specified by $dx/dt = u \pm a$. For flow in chemical nonequilibrium, of course, the appropriate sound speed a is that at fixed composition (see ref. 16, p. 300). The ordinary differential equations for the change in pressure and velocity along the characteristic Mach lines are .

$$(1/\rho a^2)(\delta^+P/\delta t) + (1/a)(\delta^+u/\delta t) = G/\rho \quad (23a)$$

and

$$(1/\rho a^2)(\delta^-P/\delta t) - (1/a)(\delta^-u/\delta t) = G/\rho \quad (23b)$$

where $\delta^+/\delta t$ and $\delta^-/\delta t$ correspond to differentials taken along right- and left-running characteristics, respectively; that is,

$$\delta^+\delta t = \partial/\partial t + (u + a) \partial/\partial x \quad (24a)$$

and

$$\delta^-\delta t = \partial/\partial t + (u - a) \partial/\partial x \quad (24b)$$

Equations (23a) and (23b) form a convenient basis for numerical calculations and, with the differential expressions along the streamline characteristics, are known as the "compatibility relations." Note that the compatibility relations given above are identical to those for a nonreacting

gas except that the term G/ρ is added to account for the effects of chemical nonequilibrium. The term G is given by (appendix B)

$$G = -\frac{w_O}{c_{pf}} \left[\frac{3}{2}R + \frac{D}{T} - \frac{R\theta_v}{T(e^{\theta_v/T} - 1)} - \frac{c_{pf}}{1 + \alpha} \right] \quad (25)$$

where c_{pf} , the specific heat at constant pressure and composition, is defined by

$$c_{pf} = \left(\frac{\partial h}{\partial T} \right)_{P,\alpha} = \left(\frac{7 + 3\alpha}{2} \right) R + \frac{(1 - \alpha)R\theta_v^2 e^{\theta_v/T}}{T^2 (e^{\theta_v/T} - 1)^2} \quad (26)$$

and w_O , the net mass rate of production of atoms, is given by

$$w_O = Wk_r(K_c[\text{O}_2][X] - [\text{O}]^2[X]) \quad (27)$$

The sound speed at fixed composition, a , is given by (ref. 16)

$$a^2 = \left(\frac{\partial h}{\partial \rho} \right)_{S,\alpha} = \left[\frac{c_{pf}}{c_{pf} - R(1 + \alpha)} \right] (1 + \alpha)R'T \quad (28)$$

Consideration of nonequilibrium reacting flows complicates the method of characteristics in that changes in concentration and entropy occur along particle paths. A determination of the conditions at a given point in a flow field must account for these variations as well as the changes in pressure and velocity prescribed by equations (23). Along a particle path (the same as a streamline in the xt plane), differences in composition and entropy are given by

$$\frac{\delta \alpha}{\delta t} = \frac{w_O}{\rho} \quad (29)$$

and

$$\frac{\delta S}{\delta t} = -\frac{1}{\rho T} \sum_k \mu_k w_k \quad (30)$$

where k represents a specific chemical species, in this case O or O_2 .

The quantity w_O is given by equation (27), and atom conservation requires

$$w_O = -w_{\text{O}_2} \quad (31)$$

The chemical potentials μ_k appearing in equation (30) are given by (appendix A)

$$\mu_{\text{O}} = -\frac{2RT}{W} \ln \left[14.419 \frac{T^{5/2}}{p_{\text{O}}} e^{-\theta_d/T} \right] \quad (32)$$

$$\mu_{\text{O}_2} = -\frac{RT}{W} \ln \left[3.714 \frac{T^{7/2}}{p_{\text{O}_2}} \frac{1}{1 - e^{-\theta_v/T}} \right] \quad (33)$$

where p_{O} and p_{O_2} are the partial pressures of oxygen atoms and molecules, respectively.

Logic of numerical solution—The present solution, like all characteristics solutions, is initiated from a set of points along a curve where flow-field properties are known, such as points 1, 2, and 3 of figure 2. First the location and then the flow-field properties of new points are computed along subsequent characteristics. In the present work, points are computed successively along left-running characteristics, as shown, so that point 4 is computed following point 3, point 5 after point 4, and so on. The location of a new point follows from the intersection of characteristic rays from two previous points (exceptions are end-wall points and shock-wave points, which are found with only one characteristic ray). The properties at each new point are computed in two steps. First, the pressure and particle velocity are found by an appropriate simultaneous solution of equations (23a) and (23b); only one of these equations together with the proper boundary conditions is required for shock-wave and end-wall points. Second, the remaining properties at the new point are found by integrating equations (29) and (30) along the particle path that passes through the new point and originates from an interpolated point a between two known points on the preceding characteristic (fig. 2). The solution continues by successive computation of rays. Details of the network construction technique are discussed in appendix C.

The conditions along an initial ray – for example, points 1, 2, and 3 – are found from a starting approximation. First, the conditions at the point of reflection, point 0, are calculated assuming chemistry frozen at $\alpha = 0$ across the reflected shock wave. Next, the properties at point 1 are established by assuming that pressure and enthalpy remain constant for a very short time along the end wall. Finally, the conditions at the boundary, point 3, are found from a simultaneous solution of equation (23b) and the appropriate shock-jump relations. Conditions at point 2 are obtained by simple linear interpolation between the conditions at points 1 and 3. A more complete description of the network-starting technique is given in appendix D.

The brief discussion here pertains to a fixed number of points along each ray. Additional points are added (by linear interpolation) along each successive ray to keep the mesh sufficiently small to assure accuracy. Furthermore, to obtain good accuracy and stability in the region immediately behind the reflected shock wave, where very large property gradients are present, a fine mesh is incorporated. The number of points in this fine mesh is variable and depends on the magnitude of the property gradients. Further details of the network-generating scheme are provided in appendix E. To further minimize errors caused by large property gradients, the solution at each point in the entire flow field is found by use of an iterative procedure. The properties first calculated for a new point are averaged with those of the known or reference points, the average values are assigned to the coordinates of the reference points, and the new point is recomputed. In addition,

equations (29) and (30) are integrated along each particle path by assuming a linear variation in pressure. Each major interval, such as from point a to point 5 of figure 2, is divided into 20 small intervals for the numerical integration (appendix C).

RESULTS AND DISCUSSION

Five solutions of reflected-shock flow fields have been obtained; the initial conditions for these solutions are summarized in table 1. Detailed results of case 1 are discussed first to establish

TABLE 1.— SUMMARY OF COMPUTER SOLUTIONS;
 $T_1 = 294^\circ \text{K}$, ALL CASES

Case	U , km/sec	P_1 , atm	β
1	3.05	2.63×10^{-3}	1
2	3.05	13.15×10^{-3}	1
3	3.05	2.63×10^{-3}	5
4	3.96	2.63×10^{-3}	1
5	2.01	2.63×10^{-3}	1

the general character of reflected-shock flow fields with nonequilibrium chemical reactions. Results from cases 2 through 5 are presented to show the effect of changing the initial pressure (case 2), the reaction-rate constant (case 3), and the incident-shock velocity (cases 4 and 5). Preliminary results are given in reference 17.

The results of the computer program are displayed in three different coordinate planes: incident-shock flow-field profiles as a function of distance behind the incident shock; end-wall properties ($x = 0$) as a function of time; and flow-field properties as a function of x for discrete times.

Case 1

Profiles of flow-field properties for the incident-shock solution of case 1 are shown in figure 3; convergence to the limiting incident-shock equilibrium conditions is apparent. The solution is typical of the dissociative relaxation of a diatomic gas. The degree of dissociation is frozen (at $\alpha = 0$) across the shock wave, and downstream of the shock all properties vary monotonically from values obtained assuming frozen composition to values corresponding to chemical equilibrium. Further, all the properties reach equilibrium on the same time scale.

Variations in several end-wall properties as a function of time are shown in figure 4, for case 1. The most striking departure from the typical behavior exhibited in a steady incident-shock flow field is evident in the pressure history. Whereas the pressure behind the incident shock wave is nearly constant (fig. 3), the pressure behind the reflected shock wave first decreases in a comparatively short time span ($\sim 0.3 \mu\text{sec}$) and then increases over a much longer time period ($\sim 100 \mu\text{sec}$). The initial decrease may be attributed to the fast chemical relaxation occurring behind the reflected shock wave, whereas the subsequent increase is a consequence of the slower relaxation behind the incident shock wave (but upstream of the reflected shock wave). Note that, except for pressure, the equilibrium property values indicated in figure 4 are for reference only and do not represent asymptotic limits at the wall.

For case 1, the relaxation time behind the incident shock wave, τ_2 , is much longer than the relaxation time behind the reflected shock $\tau_3 C$ (a graphic description of these characteristic times is shown in fig. 5). The gas in the reflected region thus quickly relaxes toward a state of local thermodynamic equilibrium corresponding to chemically frozen flow, with $\alpha = 0$, behind the incident shock and local chemical equilibrium behind the reflected shock. The pressure for such a condition is less than that corresponding to chemistry frozen at $\alpha = 0$ behind both the incident and reflect shock waves since the effect of increasing density in the reflected region (due to dissociation) must be to decrease the reflected-shock-wave velocity and hence to decrease its corresponding pressure jump.

The slow increase in pressure toward the reflected-shock "equilibrium" value is due to the nonequilibrium flow behind the incident shock wave. (A reflected-shock "equilibrium" value is defined here as the magnitude of a flow-field property when calculated assuming complete thermodynamic equilibrium behind both the incident and reflected shock waves; this is the value that applies in the flow far from the wall and is tabulated in tables of reflected-shock properties for real gases.) To a first approximation the pressure rise at the end wall occurs with the same time scale and in direct proportion to the density variation behind the incident shock wave. This finding is expected as the end wall effectively samples the incident-shock dynamic pressure, which is proportional to the density behind the incident shock wave. One consequence of this large pressure variation is that the end-wall pressure now becomes an attractive observable for reaction-rate studies. Similar behavior of the end-wall pressure was previously noted by Baganoff (ref. 10) and Johannesen et al. (ref. 11) for shock-wave reflection in vibrationally relaxing carbon dioxide.

The temperature at the end wall has an initial value corresponding to $\alpha = 0$ behind the reflected shock wave. As the relaxation proceeds, the temperature decreases rapidly toward the equilibrium value, and then increases slightly toward a final steady-state value. The presence of two time scales again is apparent as the temperature approaches a minimal value in a time that is much less than that required to approach the steady-state value. The time required for the temperature to approach its minimal value is related to the chemical relaxation time behind the reflected shock wave. This characteristic time is also evident in the relaxation of other variables, such as α and S , which are sensitive to chemical processes. The density time history can be calculated from the results plotted in figure 4; its general character consists of a continuous increase in density with an overall time scale comparable to that of the slow increase in pressure.

Another consequence of the nonsteady nature of shock-wave reflection in a relaxing gas is evident in the behavior of S , α , and T shown in figure 4 for long times on the end wall. All three of these properties approach steady-state values that are above their corresponding "equilibrium" values. A plot of the density, on the other hand, would show a steady-state level below the equilibrium value. Although the pressure eventually must approach its equilibrium value, one should not expect the final steady-state solution for the other thermodynamic properties to correspond to the usual equilibrium values (since transport processes have been omitted here). Physically, the explanation for this result is that gas particles adjacent to the end wall are processed by a stronger reflected shock wave and have different time histories than those particles that are processed by the eventual equilibrium-strength reflected shock wave. Table 2 summarizes the end-wall values at 41.4 μsec , at which time the solution for case 1 was terminated because of excessive computer time (approximately 6 hr on an IBM 7094 computer). A continuation of the computer solution would produce small additional increases in T , S , α , and ρ until the equilibrium value of pressure is attained.

TABLE 2.— COMPARISON OF END-WALL SOLUTIONS

Solution	P , atm	T , °K	S , cal/g-°K	α	ρ/ρ_1
Nonequilibrium (41.4 μ sec)	3.176	3994	2.558	0.393	63.80
Equilibrium	3.268	3919	2.501	.342	69.39
Ratio \equiv nonequilibrium/ equilibrium	.97	1.02	1.02	1.15	.92

To summarize the information presented in figure 4, the steady-state values on the end wall, for all of the thermodynamic properties except pressure, do not correspond to the usual equilibrium values. Also, the relaxation of the flow appears to be controlled by two separate relaxation times. The first, $\tau_3 C$, is a consequence of the chemical relaxation behind the reflected shock wave. The second $\tau_3 T$, the time for the pressure to reach a steady-state condition, is controlled by the relaxation time behind the incident shock wave, τ_2 . It is obvious that a steady-state solution cannot be attained behind the reflected-shock wave until the right-running characteristic that originates at the intersection of the reflected shock wave and the end of the incident-shock relaxation zone, a loosely defined point, reaches the end wall. Thus $\tau_3 T$ is approximately equal to τ_2 .

Flow-field properties for case 1 are presented in figure 6 as a function of distance from the end wall for discrete times after shock reflection. These plots are essentially "snapshots" of the various properties in the entire reflected-shock flow field taken at specified instants of time after shock reflection. Figure 6(a) shows the variation in pressure for times between 1 and 40 μ sec. Note that a plateau of near constant pressure develops within a few microseconds. The large pressure variation throughout the flow field for very short times, and near the shock for longer times, is associated with the chemical relaxation behind the reflected shock wave. The slow increase in the pressure level of the plateau can be attributed to the chemical relaxation behind the incident shock wave. The terminus of each curve in figure 6(a), away from the end wall, represents the pressure immediately behind the reflected shock wave at the specified instant of time. It can easily be shown that since a pressure gradient cannot be sustained in the flow field, the pressure must approach the equilibrium value throughout the flow field for long times after reflection. Thus, in a coordinate system that is fixed relative to the reflected shock, for long times after reflection the flow must show behavior similar to that of an incident-shock solution with upstream properties corresponding to the equilibrium conditions behind the actual incident shock wave. Downstream of the reflected shock wave, of course, there will ultimately be a steady nonequilibrium relaxation zone bounded by an over-growing region of gas in chemical equilibrium and at rest with respect to the shock tube.

The spatial variation in entropy behind the reflected shock wave is shown in figure 6(b). The entropy at $x=0$ quickly exceeds the equilibrium value (fig. 4), and figure 6(b) shows that it extends into the flow field in the form of an excess-entropy layer bounded by the end wall. As the shock moves away from the end wall, this layer becomes of nearly fixed extent at times greater than 10 μ sec and a steady-state entropy value is approached outside the layer that is asymptotic to the equilibrium value. The large entropy variations near the shock wave are a consequence of the chemical relaxation immediately behind the reflected shock.

Spatial distributions of the degree of dissociation and of temperature are shown in figure 6(c) and (d), respectively. Note that throughout the fully developed excess-entropy layer both α and T have values that are higher than their corresponding equilibrium levels. However, further from the end wall, steady-state plateaus begin to develop, at times greater than about 10 μsec , wherein the properties approach their equilibrium values. Of course, large variations in α and T occur adjacent to the shock in the reflected-shock relaxation zone. As the flow properties upstream of the reflected shock become increasingly uniform, the relaxation profiles downstream of the reflected shock approach steady-state distributions (as viewed in shock-fixed coordinates). After 40 μsec , for example, the reflected shock has propagated through the incident-shock relaxation zone a distance of about 14 cm and the incident-shock properties have nearly reached their equilibrium values (fig. 3).

Spatial variations in density are shown in figure 6(e) for the same time increments. The results indicate a general increase in density with time at all flow-field positions, although the final density throughout the entropy layer and near the shock front remains at a lower level than the equilibrium values. Because the density is strongly coupled to pressure, no steady-state value is approached in the time span shown on the figure. This coupling between pressure and density has a simple physical interpretation. The rising pressure compresses the gas, thus increasing its energy, but the heat-sink effect of the dissociation energy acts to hold the temperature and degree of dissociation nearly constant once "local" chemical equilibrium has been reached. Subsequent changes in pressure are thus accompanied by nearly proportionate changes in density.

Measurements of density profiles have been used extensively to obtain rate information behind incident shock waves. The variation in density behind the reflected shock wave, at a fixed distance from the end wall, could also be used to infer reaction rates, but care must be exercised in interpreting the data since the density profiles are different functions of time for different observation stations. The decrement in density associated with the excess-entropy layer should be detectable in a density measurement; in fact, Johannessen et al. (ref. 11) have obtained interferometer records exhibiting such a density decrease, partially masked by end-wall heat-transfer effects, for the vibrational relaxation of carbon dioxide behind a reflected shock wave.

A boundary condition for "equilibrium" calculations behind reflected shock waves is that the flow velocity, relative to the shock-tube end wall, vanishes throughout the flow field. However, as mentioned earlier, for nonequilibrium calculations this boundary condition can be imposed *only* at the end wall. Spatial variations of velocity are shown in figure 6(f). Although a large gradient in flow velocity exists near the shock wave, except for small times the flow velocity approaches zero over a major portion of the flow field, as one would expect since the pressure gradient (spatial) is so small.

Strehlow and Cohen (ref. 5) have shown that vibrational relaxation in nitrogen and oxygen causes an initial deceleration in the velocity of the reflected shock wave, relative to the shock tube. Similar behavior is shown in figure 7 for the case of dissociation of a diatomic molecule. The reflected shock velocity initially (at $x = 0$) has a value corresponding to $\alpha = 0$ behind the reflected shock wave. However, the velocity quickly decelerates to a minimum value that is less than the equilibrium value and corresponds closely to the value computed under the assumptions of $\alpha = 0$ behind the incident shock wave and equilibrium chemistry behind the reflected shock wave. After reaching this minimum, the reflected-shock velocity increases slowly and should eventually reach the equilibrium value.

The foregoing figures present a complete description of the nonequilibrium reflected-shock flow field for case 1. Primary conclusions are: (1) two relaxation times control the flow behind the reflected shock; and (2) an excess-entropy layer is formed, near the end wall, in which the entropy and all other thermodynamic variables except pressure differ from their "equilibrium" values. The excess of entropy in this layer will not diminish, because within the assumptions of the present model there is no mechanism available to drive the entropy back to its equilibrium value. In the real case, of course, transport processes are present and would act to smooth out all existing flow-field nonuniformities.

Capiaux and Washington (ref. 18) have investigated the analogous problem of nonequilibrium hypersonic flow of a dissociating gas past a semi-infinite wedge with a sharp leading edge. Their calculations also predict the formation of an entropy layer, located above the surface of the wedge, but they did not discuss the magnitude of the steady-state surface entropy in comparison to the equilibrium value. However, for their case, wherein the shock wave was convex, one also would expect that the surface entropy should exceed the equilibrium value appropriate for the deflection angle of the wedge.

Cases 2 - 5

With the general features of a nonequilibrium reflected-shock flow field understood, the results of cases 2 through 5 can be used in evaluating the influence of parameters such as initial pressure, reaction-rate constant, and shock velocity. We first consider the computed incident-shock flow fields for cases 2 through 5 (fig. 8) and compare them with the results of case 1 (fig. 3). Case 2 illustrates the effects of a fivefold increase in P_1 , with U and β held at their case 1 values. The primary effect is simply a decrease in the length of the relaxation zone, as might be expected because of the resultant increase in the magnitude of the rate equation (eqs. (7) and (11-13)). From a physical viewpoint, an increase in initial pressure increases the collision frequency of the molecular species, leading to a faster rate of reaction. Within the framework of the present model, some thermodynamic properties immediately behind the shock front (such as T , α , ρ/ρ_1 , and P/P_1) are independent of the initial pressure and hence take the same values for cases 1 and 2. The equilibrium conditions are pressure dependent to some extent, however, because the equilibrium degree of dissociation is a function of temperature and pressure. The net changes for case 2 compared to case 1 equilibrium values are small decreases in α and ρ/ρ_1 and a small increase in T ; the equilibrium pressure for case 2 is almost exactly five times that of case 1.

Case 3 demonstrates the effects of increasing the rate constant by a factor of 5 with the initial pressure and shock velocity held at their case 1. Since the rate parameter β does not enter the calculation of properties at any one flow-field point, but only affects the distance between adjacent flow-field points (eqs. (7)-(9), (17), and (18)), the flow-field profiles of case 3 are identical to those of case 1 except for a difference in the spatial scale of exactly a factor of 5.

Cases 4 and 5 show the effects of changing the incident-shock speed U with P_1 and β fixed at their standard values (fig. 8). In case 4, as might be expected for the case of a stronger shock wave, the variations in all the properties are larger across the relaxation zone and the temperature level is generally higher. The increase in the equilibrium degree of dissociation is especially notable; this parameter is quite sensitive to the energy content of the gas, which in turn depends strongly

on the magnitude of U . A further point is that the overall relaxation length is seen to decrease with increasing shock speed, primarily because of the strong dependence of the rate constant on temperature. Case 5 represents the case of a weak shock wave, which causes very little dissociation. Accordingly, only small variations in property values are present in the incident-shock relaxation zone. The low temperatures are responsible for the great increase in the scale of the relaxation zone. Case 5 thus presents, effectively, the limiting situation of shock-wave reflection into a uniform nonreacting flow.

Figure 9 compares end-wall properties plotted as a function of time after reflection for cases 2 through 5. With minor variations, discussed below, the results are similar to those of case 1. Two characteristic times are present in each case, for example, and consistent deviations are found between the steady-state and equilibrium property values. To avoid excessive computer time, the solutions for all five cases were terminated prior to reaching a true steady state, but the final values of all properties can be estimated from the results shown. The computed pressure should approach asymptotically to the equilibrium value in all cases.

The results for case 2, which illustrate the influence of increased initial pressure, differ from those of case 1 primarily in the time to reach steady conditions. The time scale of the entire solution is reduced because of the increased reaction-rate magnitude downstream of the reflected shock wave and the decreased spatial extent of the relaxation zone upstream of the reflected shock wave (fig. 8). For case 2, the general level of the pressure is higher than for case 1, and because of its dependence on pressure, the entropy is smaller. The equilibrium property values for case 2 differ slightly from those for case 1, but the deviations between steady-state and equilibrium values are nearly the same for both cases.

The results for case 3 (fig. 9) are identical to those of case 1 (fig. 4) except for a factor of 5 change in the time scale. Thus, the case 3 results confirm that the end-wall-properties solution, as well as the incident-shock flow-field solution, scales inversely with the magnitude of β . Justification for this result follows from a consideration of the reflected-shock flow-field computation technique (appendix C) and an understanding of the incident-shock flow-field dependence on β .

The property-time histories of case 4 (fig. 9) show larger variations than all other cases, throughout the equilibration process, in all the properties plotted. This is the expected result for a stronger shock wave causing increased dissociation. In addition, the increase in shock strength leads to larger deviations between steady-state and equilibrium property values. The time to reach steady-state conditions is less than that for case 1, as might be expected since the overall time is coupled to the relaxation time behind the incident shock wave τ_2 , and τ_2 is less for case 4 than for case 1. Another interesting feature of case 4 is the absence of an initial decay in end-wall pressure prior to the increase in pressure associated with chemical relaxation behind the incident shock. The initial period of near-constant pressure is actually a result of two competing effects. First, the chemical relaxation behind the reflected shock wave introduces a negative pressure gradient in time (with a time scale τ_{3C}) as the flow relaxes toward chemical equilibrium. Second, the gradient in flow properties behind the incident shock wave induces a positive pressure gradient (with an approximate time scale τ_2) on the end wall. Case 4 represents a solution wherein the initial values of these two gradients nearly cancel and no dip in pressure occurs on the end wall — that is, there is a strong interaction with the incident-shock flow field. A strong interaction is thus to be

expected whenever the relaxation times $\tau_3 C$ and τ_2 are not widely separate. In general, the difference between $\tau_3 C$ and τ_2 lessens, and the extent of the interaction grows, with increasing shock strength.

The results for case 5 (fig. 9) are typical of end-wall solutions for shock waves producing only a small degree of dissociation. In such cases, there is a weak interaction between incident- and reflected-shock flow fields, and the characteristic times $\tau_3 C$ and $\tau_3 T$ are completely distinct. The results shown in figure 9, however, are restricted to times of order $\tau_3 C$ and do not approach the scale of τ_2 or $\tau_3 T$. It appears that local chemical equilibrium is reached in approximately $10^2 \mu\text{sec}$, as evidenced by the behavior of all variables plotted, and the small increase in pressure shown for times greater than $10^2 \mu\text{sec}$ indicates the onset of the influence of the incident-shock relaxation. The relaxation time τ_2 is of the order of $10^4 \mu\text{sec}$ for this case, so end-wall conditions at $10^2 \mu\text{sec}$ should correspond closely to the limiting case of shock-wave reflection into a uniform, nonreacting flow. Note that an excess-entropy layer has already formed; the magnitudes of T, S , and α at $10^2 \mu\text{sec}$ are greater than their equilibrium values, so the formation of an entropy layer does not depend solely on the propagation of the reflected shock wave through a nonuniform upstream region. The effect of the incident-shock relaxation zone will be to greatly increase the spatial extent of the entropy layer, however, and to a lesser extent to increase the deviations between the steady-state and equilibrium wall-property values.

It has been shown, in figures 4 and 9, that large variations in end-wall pressure may be present during shock-wave reflection. Pressure is a convenient quantity for measurement, but its suitability as a diagnostic tool in reaction-rate studies depends in part on the sensitivity of end-wall pressure to experimental parameters and the chemical reaction rate. For the purpose of further illustrating this sensitivity, the end-wall pressure histories for all five cases are replotted in figure 10, where, for convenience, the pressure coordinate has been normalized by the frozen ($\alpha = 0$) reflected-shock pressure for each solution. From the results shown here (and in figs. 4 and 9), it is clear that the wall pressure is much more sensitive to the influence of chemical relaxation behind the incident shock wave than to the shorter-term effects of relaxation in the reflected region. Furthermore, it is obvious that the magnitude of the pressure variation following reflection increases with shock strength (compare the results for cases 4 and 5, for example) and that the time scale of the pressure history, for a fixed-speed shock, is sensitive to the parameters of initial pressure and rate constant (cf. cases 1-3). Thus it appears that measurements of wall pressure would provide an attractive method for studying reaction rates behind moderately strong or strong incident shock waves.

Flow-field plots at discrete times after reflection are presented for cases 2 through 5 in figures 11 through 14, respectively. The format is the same as that used for case 1 in figure 4; since the results are generally similar in character to those of case 1, only new and significant features are discussed here. The distinguishing characteristic of the plots for cases 2 through 4 is the reduction in the time required to reach near-steady conditions, the decrease resulting from the dependence of the relaxation time on the pressure, rate-constant multiplier, and shock velocity, respectively, for cases 2, 3, and 4. Of course, the reduction in relaxation time is also responsible for diminishing the entropy-layer thickness. One important result, seen from a comparison of figures 4 and 12, is that the reflected-shock flow-field distributions scale in a simple way with the value of β . That is, all property values at the wall and at the shock front for case 3, at any time t , match exactly those for case 1 at the time $5t$ (recall that $\beta = 1$ for case 1 and $\beta = 5$ for case 3). At these times, the distances between the wall and the shock front for cases 1 and 3 differ by a

factor of 5, as do the gradients in each flow property. Thus, the entire shock-reflection solution, including the reflected-shock flow-field distributions, scales in a simple manner with the value of the rate-constant multiplier β .


Several interesting features appear in the results plotted for case 5 (fig. 14). Since the time scale of the plots ($t \leq 200 \mu\text{sec}$) corresponds roughly to the relaxation time in the reflected region, the results for case 5 illustrate more clearly than those for the previous cases the progressive behavior of each property during this relaxation process. The results are typical of shock-wave reflection with chemical nonequilibrium downstream of the reflected shock and nonreacting flow upstream. The curves for pressure indicate that at about 100 μsec a minimum is reached for the plateau pressure level, and for larger times an increase in pressure level is expected. The plots for the entropy distribution confirm that after a time of 200 μsec the entropy layer is not yet fully developed, since no plateau in entropy is yet visible, and the entropy level remains higher than the equilibrium value. In fact, the entire reflected-shock flow field is still slightly out of equilibrium after 200 μsec , as evidenced by the continuing changes in the degree of dissociation and temperature throughout the reflected region. After local equilibrium is achieved, the values of all properties will change further (although slowly) because of the effects of nonequilibrium behind the incident shock wave. These changes will be small because of the nearly negligible degree of dissociation throughout the incident-shock relaxation zone.

Figure 15 compares results of cases 2 through 5 for the reflected shock velocity plotted as a function of distance from the end wall. The results are consistent with those of case 1 (fig. 7) with one exception: In case 5, the computations were stopped before a minimum in the shock-velocity history was reached. Further calculations should have shown a further decrease in reflected-shock velocity to a minimum value (less than the equilibrium value) followed by a slow, asymptotic rise toward the equilibrium value.

CONCLUDING REMARKS

In contrast to nonequilibrium incident-shock flow fields, large temporal variations in pressure may occur behind reflected shock waves. The magnitude of this pressure change and the sensitivity of its time scale to experimental variables make it a useful quantity for measurement in reaction-rate studies.

The relaxation process behind a reflected shock wave exhibits two separate time scales. Properties that are sensitive to the chemical state, such as entropy, temperature, and the degree of dissociation, relax in a time τ_{3C} that is controlled by the chemical reaction rate behind the reflected shock wave. Properties that are sensitive to fluid-dynamic phenomena, such as pressure and density, relax in a time τ_{3T} that is controlled by the time to obtain steady-state conditions behind the incident shock wave; τ_{3T} is usually much greater than τ_{3C} .



An excess-entropy layer of gas is formed, adjacent to the end wall, in which all of the thermodynamic properties, except pressure, differ significantly from their usual equilibrium conditions as a steady-state solution is approached.

Ames Research Center
National Aeronautics and Space Administration
Moffett Field, Calif., 94035, April 12, 1972

APPENDIX A

SIMPLIFIED EXPRESSIONS FOR THE CHEMICAL EQUILIBRIUM CONSTANT AND THE CHEMICAL POTENTIALS

The equilibrium constant for a dissociating, homonuclear diatomic gas may be written (ref. 16, p. 166)

$$K_c = \frac{[A]^2}{[A_2]} \Big|_{\text{eq}} = \frac{(Q^A/V)^2}{\bar{N}(Q^{A_2}/V)} \quad \text{moles/cm}^3 \quad (\text{A1})$$

where A and A_2 denote atomic and molecular species, respectively, Q^A and Q^{A_2} are the atomic and molecular partition functions, V is the volume of the system and \bar{N} is Avogadro's number.

For the atoms, the complete partition function is simply the product of the translational and electronic partition functions

$$Q^A = Q_{\text{tr}}^A Q_{\text{el}}^A e^{-\theta_d/2T} \quad (\text{A2})$$

The exponential factor results from choosing as the reference energy level the ground vibrational and electronic state of the molecule. The translational partition function is given by

$$Q_{\text{tr}}^A = \left(\frac{2\pi mkT}{h^2} \right)^{3/2} V \quad (\text{A3})$$

where m is the mass of the atom, and k and h are the Boltzmann and Planck constants, respectively. The electronic partition function is given by

$$Q_{\text{el}}^A = \sum_i g_i e^{-\theta_{\text{el},i}/T} \quad (\text{A4})$$

where the g_i are degeneracy factors for the levels of energy characterized by the temperatures $\theta_{\text{el},i}$.

For the molecules, the complete partition function is the product of the translational, rotational, vibrational, and electronic partition functions

$$Q^{A_2} = Q_{\text{tr}}^{A_2} Q_{\text{rot}}^{A_2} Q_{\text{vib}}^{A_2} Q_{\text{el}}^{A_2} \quad (\text{A5})$$

The translational and electronic partition functions take the same form as expressed above for the atoms, but are evaluated with the molecular mass ($2m$) and molecular electronic-level parameters. The rotational and vibrational partition functions are (ref. 16)

$$Q_{\text{rot}}^{A_2} = \frac{T}{2\theta_r} \quad (\text{A6})$$

and

$$Q_{\text{vib}}^{A_2} = \left(1 - e^{-\theta_v/T}\right)^{-1} \quad (\text{A7})$$

where θ_r and θ_v are characteristic rotational and vibrational temperatures.

A simplified expression for the equilibrium constant in oxygen can now be formed by substituting appropriate values for the constants involved in the expressions above. Assuming approximate values for the electronic partition functions of $Q_{\text{el}}^O = 8.8$ and $Q_{\text{el}}^{O_2} = 3.3$ (reasonably valid over the temperature range of interest in this work), one finds that

$$K_c(T) = 0.666 (T)^{1/2} \left(1 - e^{-\theta_v/T}\right) e^{-\theta_d/T} \text{ moles/cm}^3 \quad (\text{A8})$$

The chemical potential of each component in a mixture of thermally perfect gases is given by (ref. 16)

$$\mu_i = -\frac{RT}{W_i} \ln\left(\frac{Q_i^t}{N_i}\right) \text{ cal/g} \quad (\text{A9})$$

where Q_i^t is the complete partition function of species i , W_i is the molecular weight, and N_i is the number of particles of species i in the system.

From the above discussion of partition functions, and again choosing the ground molecular state as the reference energy level, one can immediately write

$$\frac{Q^A}{N_A} = \left[\frac{2\pi mkT}{h^2}\right]^{3/2} \left(\frac{V}{N_A}\right) Q_{\text{el}}^A e^{-\theta_d/2T} \quad (\text{A10})$$

and

$$\frac{Q^{A_2}}{N_{A_2}} = \left[\frac{4\pi mkT}{h^2}\right]^{3/2} \left(\frac{V}{N_{A_2}}\right) \left(\frac{T}{2\theta_r}\right) \left(1 - e^{-\theta_v/T}\right)^{-1} Q_{\text{el}}^{A_2} \quad (\text{A11})$$

Simplified expressions for oxygen are again formed by substituting values for the constants involved and noting that $V/N_A = kT/p_A$ (where p_A is the partial pressure of the atoms, in dynes/cm²):

$$\frac{Q^O}{N_O} = 14.606 \times 10^6 \left(\frac{T^{5/2}}{p_O}\right) e^{-\theta_d/2T} \quad (\text{A12})$$

and

$$\frac{Q^{O_2}}{N_{O_2}} = 3.762 \times 10^6 \left(\frac{T^{7/2}}{p_{O_2}} \right) \left(1 - e^{-\theta_v/T} \right)^{-1} \quad (\text{A13})$$

By expressing the partial pressures in units of atmospheres (rather than dynes/cm²), one obtains final simple expressions

$$\mu_O = - (RT/16) \ln \left[14.419(T^{5/2}/p_O) e^{-\theta_d/2T} \right] \quad \text{cal/g} \quad (\text{A14})$$

and

$$\mu_{O_2} = - (RT/32) \ln \left[3.714(T^{7/2}/p_{O_2}) \left(1 - e^{-\theta_v/T} \right)^{-1} \right] \quad \text{cal/g} \quad (\text{A15})$$

The partial pressures are related to the total pressure P by

$$p_O = \frac{2\alpha}{1 + \alpha} P \quad (\text{A16})$$

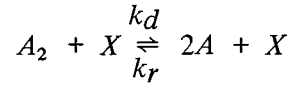
and

$$p_{O_2} = \frac{1 - \alpha}{1 + \alpha} P \quad (\text{A17})$$

APPENDIX B

METHOD OF CHARACTERISTICS FOR ONE-DIMENSIONAL MOTION OF A DISSOCIATING, HOMONUCLEAR DIATOMIC GAS

The characteristic equations for pressure and mass velocity in a reacting gas are formulated in the same manner as that used for the case of a nonreacting gas – by manipulating general thermodynamics relations together with the conservation equations. For a homonuclear diatomic gas undergoing the reaction



where X is any collision partner, the pertinent relations (see earlier text for notation) are as follows:

Conservation of mass

$$\frac{D\rho}{Dt} + \rho \frac{\partial u}{\partial x} = 0 \quad (\text{B1})$$

Conservation of momentum

$$\rho \frac{Du}{Dt} + \frac{\partial P}{\partial x} = 0 \quad (\text{B2})$$

Equation of state

$$\rho = \rho(P, S, \alpha) \quad (\text{B3})$$

Rate of entropy production owing to chemical nonequilibrium

$$\frac{DS}{Dt} = - \frac{1}{\rho T} \sum_i \mu_i w_i = - \frac{1}{\rho T} (\mu_A - \mu_{A_2}) w_A \quad (\text{B4})$$

Rate of production of atom mass density owing to chemical reaction

$$w_A = \rho \frac{D\alpha}{Dt} = W \{k_d [A_2] [X] - k_r [A]^2 [X]\} \quad (\text{B5})$$

Speed of sound at constant chemistry

$$a^2 = \left(\frac{\partial P}{\partial \rho} \right)_{S, \alpha} \quad (\text{B6})$$

Equation (B3) may be written in differential form as

$$\frac{D\rho}{Dt} = \left(\frac{\partial \rho}{\partial P} \right)_{S, \alpha} \frac{DP}{Dt} + \left(\frac{\partial \rho}{\partial S} \right)_{\alpha, P} \frac{DS}{Dt} + \left(\frac{\partial \rho}{\partial \alpha} \right)_{P, S} \frac{D\alpha}{Dt} \quad (\text{B7})$$

However, from the combined first and second laws of thermodynamics for this reacting system

$$dh = TdS + \frac{dP}{\rho} + (\mu_{A_1} - \mu_{A_2}) d\alpha \quad (\text{B8})$$

so that

$$\left(\frac{\partial h}{\partial S} \right)_{\alpha, P} = T \quad (\text{B9})$$

and

$$\left(\frac{\partial \rho}{\partial S} \right)_{\alpha, P} = \left(\frac{\partial \rho}{\partial h} \right)_{\alpha, P} \left(\frac{\partial h}{\partial S} \right)_{\alpha, P} = \left(\frac{\partial \rho}{\partial h} \right)_{\alpha, P} T \quad (\text{B10})$$

In addition, h may be written in terms of P , α , and ρ so that

$$dh = \left(\frac{\partial h}{\partial P} \right)_{\alpha, \rho} dP + \left(\frac{\partial h}{\partial \alpha} \right)_{\rho, P} d\alpha + \left(\frac{\partial h}{\partial \rho} \right)_{P, \alpha} d\rho \quad (\text{B11})$$

An inspection of this relation and the preceding differential expression for h allows one to write

$$\left(\frac{\partial \rho}{\partial \alpha} \right)_{P, S} = \frac{(\mu_{A_1} - \mu_{A_2}) - (\partial h / \partial \alpha)_{P, \rho}}{(\partial h / \partial \rho)_{P, \alpha}} \quad (\text{B12})$$

Equation (B7) may now be rewritten as

$$\frac{D\rho}{Dt} = \left(\frac{\partial \rho}{\partial P} \right)_{S, \alpha} \frac{DP}{Dt} + T \left(\frac{\partial \rho}{\partial h} \right)_{P, \alpha} \frac{DS}{Dt} + \frac{(\mu_{A_1} - \mu_{A_2}) - (\partial h / \partial \alpha)_{P, \rho}}{(\partial h / \partial \rho)_{P, \alpha}} \frac{D\alpha}{Dt} \quad (\text{B13})$$

Upon substituting equations (B4), (B5), and (B6), one obtains

$$\frac{D\rho}{Dt} = \frac{1}{a^2} \frac{DP}{dt} - \frac{(\partial h/\partial \alpha)_{P,\rho}}{(\partial h/\partial \rho)_{P,\alpha}} \frac{w_A}{\rho} \quad (\text{B14})$$

The characteristics equations can now be formed by substituting equation (B14) into equation (B1), multiplying equation (B2) by $1/a$, and first adding and then subtracting the resulting forms of these two equations. The results are

$$\frac{1}{a^2} \left[\frac{\partial P}{\partial t} + (u+a) \frac{\partial P}{\partial x} \right] + \frac{\rho}{a} \left[\frac{\partial u}{\partial t} + (u+a) \frac{\partial u}{\partial x} \right] = G \quad (\text{B15})$$

and

$$\frac{1}{a^2} \left[\frac{\partial P}{\partial t} + (u-a) \frac{\partial P}{\partial x} \right] - \frac{\rho}{a} \left[\frac{\partial u}{\partial t} + (u-a) \frac{\partial u}{\partial x} \right] = G \quad (\text{B16})$$

where

$$G = \frac{(\partial h/\partial \alpha)_{P,\rho}}{(\partial h/\partial \rho)_{P,\alpha}} \frac{w_A}{\rho} \quad (\text{B17})$$

These two equations determine the rate of change of pressure and mass velocity along the right- and left-running characteristic lines specified by $dx/dt = u \pm a$.

The characteristics equations can be cast into an abbreviated form with the notation

$$\frac{\delta^+}{\delta t} = \frac{\partial}{\partial t} + (u+a) \frac{\partial}{\partial x} \quad (\text{B18})$$

and

$$\frac{\delta^-}{\delta t} = \frac{\partial}{\partial t} + (u-a) \frac{\partial}{\partial x} \quad (\text{B19})$$

so that

$$\frac{1}{\rho a^2} \frac{\delta^+ P}{\delta t} + \frac{1}{a} \frac{\delta^- u}{\delta t} = \frac{G}{\rho} \quad (\text{B20})$$

and

$$\frac{1}{\rho a^2} \frac{\delta^- P}{\delta t} - \frac{1}{a} \frac{\delta^- u}{\delta t} = \frac{G}{\rho} \quad (\text{B21})$$

Thus $\delta^+/\delta t$ and $\delta^-/\delta t$ correspond to differentials along the right- and left-running characteristics, respectively. Equations (B20) and (B21) can be used to calculate changes in P and u throughout characteristic network, once an appropriate form for the term G is obtained. Note that $G \equiv 0$ when $w_A = 0$ in which circumstances the forms of equations (B20) and (B21) reduce to the standard equations used for isentropic flow. In the case of chemical equilibrium, the sound speed a takes on its equilibrium value.

An explicit form for G is established by utilizing the thermal and caloric equations of state (eqs. (5) and (6) in text). From these expressions, one can write

$$\left(\frac{\partial h}{\partial \rho}\right)_{P,\alpha} = \left(\frac{\partial h}{\partial T}\right)_{P,\alpha} \left(\frac{\partial T}{\partial \rho}\right)_{P,\alpha} = c_{pf} \left(\frac{-T}{\rho}\right) \quad (\text{B22})$$

where

$$c_{pf} = \left(\frac{\partial h}{\partial T}\right)_{P,\alpha}$$

is the specific heat at constant pressure and composition; that is,

$$c_{pf} = \left[\frac{7 + 3\alpha}{2} R + \frac{(1 - \alpha) R (\theta_v/T)^2 e^{\theta_v/T}}{(e^{\theta_v/T} - 1)^2} \right] \quad \text{cal/initial mole} - ^\circ\text{K} \quad (\text{B23})$$

One can also write

$$\begin{aligned} \left(\frac{\partial h}{\partial \alpha}\right)_{P,\rho} &= \left(\frac{\partial h}{\partial \alpha}\right)_T + \left(\frac{\partial h}{\partial T}\right)_\alpha \left(\frac{\partial T}{\partial \alpha}\right)_{P,\rho} \\ &= \left(\frac{\partial h}{\partial \alpha}\right)_T + c_{pf} \left(\frac{-T}{1 + \alpha}\right) \end{aligned} \quad (\text{B24})$$

where

$$\left(\frac{\partial h}{\partial \alpha}\right)_T = \left(\frac{3}{2} RT - \frac{R\theta_v}{e^{\theta_v/T} - 1} + D\right) \quad (\text{B25})$$



Substituting the above results in equation (B17), one finds that G is simply given by

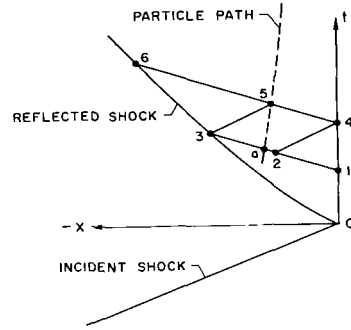
$$G = - \left[\left(\frac{3}{2} R + \frac{D}{T} - \frac{R \theta_v/T}{e^{\theta_v/T} - 1} \right) - \frac{c_{pf}}{1 + \alpha} \right] \frac{w_A}{c_{pf}} \quad \text{g/cm}^3\text{-sec} \quad (\text{B26})$$

where c_{pf} is specified by equation (B23).

APPENDIX C

NETWORK CONSTRUCTION TECHNIQUE

As in all characteristic solutions, the present solution proceeds from a known set of points in the flow field. Disregarding the starting approximation for the time being (appendix D), the solution proceeds from the known set of properties along the left-running characteristic ray 1-3, as shown in sketch (a). The properties on a subsequent ray, ray 4-6, are obtained from those on the initial ray by calculating three types of points: (1) end wall, (2) interior, and (3) shock wave.



Sketch (a).—Characteristic network construction.

End-Wall Point

The procedure required to obtain values of the flow-field variables at an end-wall point, say point 4, is as follows:

1. The location of point 4 in the xt plane is established geometrically by the intersection of the right-running characteristic from point 2, slope $dx/dt = (u + a)_2$ and the end wall at $x = 0$.
2. The pressure P_4 is obtained by solving the finite-difference form of equation (23a):

$$\left(\frac{1}{\rho a^2} \right)_2 \frac{P_4 - P_2}{t_4 - t_2} - \frac{1}{a_2} \frac{u_2}{t_4 - t_2} = \left(\frac{G}{\rho} \right)_2 \quad (C1)$$

since the velocity at the end wall u_4 is zero.

3. The values for the degree of dissociation α_4 and the entropy S_4 are found by solving the finite-difference forms of equations (29) and (30) along the end wall, which is the location of a particular particle path. To minimize accumulative errors, we first divide the overall time interval $t_4 - t_1$ into 20 equal subintervals (throughout which the pressure is assumed to vary linearly from P_1 to P_4), and then apply equations (29) and (30) to each subinterval. The appropriate forms of equations (29) and (30), respectively, are

$$\frac{\alpha_j - \alpha_{j-1}}{t_j - t_{j-1}} = \left(\frac{w_0}{\rho} \right)_{j-1} \quad (C2)$$

and

$$\frac{S_i - S_{i-1}}{t_i - t_{i-1}} = - \left[\frac{1}{\rho T} \sum_k \mu_k w_k \right]_{i-1} \quad (C3)$$

where $i - 1$ represents the point along the particle path at which the calculations have been completed and the properties are known, and i is the subsequent point at which time and pressure are known and all other properties are to be determined.

4. Using the values of P , α , and S at each point i , the temperature can be found by satisfying the following equation for entropy (as a function of T , α , and P (in atm)) implicitly:

$$S = \frac{R(1 + \alpha)}{W} \left[\sum_k N_k \left(\frac{S^0}{R} \right)_k - \sum_k N_k \ln N_k - \ln P \right] \quad (C4)$$

where N_k are mole fractions of the species involved,

$$N_{\text{O}} = \frac{2\alpha}{1 + \alpha} \quad \text{and} \quad N_{\text{O}_2} = \frac{1 - \alpha}{1 + \alpha}$$

and $(S^0/R)_k$ is the dimensionless entropy of species k evaluated for a pressure of 1 atm; that is,

$$\left(\frac{S^0}{R} \right)_{\text{O}} = \frac{5}{2} + \frac{\theta_d}{2T} + \ln \left(14.419 T^{5/2} e^{-\theta_d/2T} \right)$$

and

$$\left(\frac{S^0}{R} \right)_{\text{O}_2} = \frac{7}{2} + \frac{\theta_v e^{-\theta_v/T}}{T (1 - e^{-\theta_v/T})} + \ln \left[\frac{3.714 T^{7/2}}{1 - e^{-\theta_v/T}} \right]$$

The calculations continue until α , S , and T are found at point 4. Other desired thermodynamic quantities can now be computed directly in terms of the known properties.

Interior Point

The solution of an interior point, say point 5 in sketch 1, proceeds in much the same manner as described for an end-wall point.

1. Point 5 is located geometrically by the intersection of a right-running characteristic from point 3, slope $dx/dt = (u + a)_3$, and the left-running characteristic from point 4, slope $dx/dt = (u - a)_4$.

2. The pressure and velocity at point 5, P_5 and u_5 , are found by solving the following two equations simultaneously:

$$\left(\frac{1}{\rho a^2}\right)_3 \frac{P_5 - P_3}{t_5 - t_3} + \frac{1}{a_3} \frac{u_5 - u_3}{t_5 - t_3} = \left(\frac{G}{\rho}\right)_3 \quad (\text{C5})$$

and

$$\left(\frac{1}{\rho a^2}\right)_4 \frac{P_5 - P_4}{t_5 - t_4} - \frac{1}{a_4} \frac{u_5 - u_4}{t_5 - t_4} = \left(\frac{G}{\rho}\right)_4 \quad (\text{C6})$$

3. The degree of dissociation and the entropy at point 5 are found by the technique described in step 3 for the end-wall point – that is, by applying the finite-difference forms of equations (29) and (30) to 20 subintervals along the particle path passing through point 5. The origin of this particle path, point a, is found by searching along the characteristic segment between points 2 and 3 (using linear interpolation) for a value of particle velocity that when averaged with the known velocity at point 5, corresponds to passage through point 5. The values of P , T , and α at point a are found by linear interpolation between the known properties at points 2 and 3. Values of other necessary quantities at point a, such as ρ , S , w_{O} , μ_{O} , and μ_{O_2} , are then computed from the interpolated values of P , T , and α .

4. The temperature at each subinterval point along the particle path is found from a knowledge of P , α , and S at the corresponding point, as described for the end-wall point.

Shock-Wave Point

Values of the flow-field variables at a shock-wave point are obtained as follows:

1. Coordinates of a shock-wave point, point 6, are found from the intersection of a left-running characteristic from point 5, slope $dx/dt = (u - a)_5$, and the reflected shock wave from point 3. The velocity of the reflected shock wave is assumed to be constant between points along the shock wave trajectory, and is allowed to change discontinuously at each shock-wave point.

2. Flow properties in front of the reflected shock wave are found from the appropriate position in the incident shock-wave solution – that is, at a distance s behind the incident shock where (for point 6)

$$s_6 = -x_6 + Ut_6$$

3. Pressure and particle velocity immediately downstream of the shock, at point 6, are found by solving

$$\left(\frac{1}{\rho a^2}\right)_5 \frac{P_6 - P_5}{t_6 - t_5} - \frac{1}{a_5} \frac{u_6 - u_5}{t_6 - t_5} = \left(\frac{G}{\rho}\right)_5 \quad (\text{C7})$$

simultaneously with the Rankine-Hugoniot jump conditions across the reflected shock wave. The only boundary condition imposed on the solution of this point is that the degree of dissociation remains invariant across the reflected shock wave. The additional thermodynamic properties needed

and a new value for the reflected shock speed follow directly from the conservation equations (applied across the reflected shock) and the state relations.

Methods of Minimizing Error

The flow-field solution is continued by successive computation of rays. Although the description herein is for a fixed number of points (each subsequent ray increases the number of points per ray by one), additional points may be added (by interpolation) along each successive ray to keep the mesh sufficiently small to preserve accuracy. Furthermore, to obtain good accuracy and stability in the region immediately behind the reflect shock wave, where very large property gradients are present, a fine mesh is incorporated into this region of the network (see appendix E). The number of points in this fine mesh is variable and depends on the magnitude of the property gradients.

In addition to the procedures described above for calculating the three types of points, the solution at each point in the entire flow field is iterated once. That is, in order to minimize errors due to large property gradients, it is more efficient to iterate the solution of each new flow-field point once than to use a finer network of points and not to iterate. The technique simply involves averaging the properties of a newly calculated point with those of the known or reference points, assigning the average values to the coordinates of the known points, and recomputing the position and properties of the new point.

Iteration at each flow-field point and the use of a fine mesh scheme near the shock wave have proven effective methods of minimizing errors (e.g., the so-called entropy diffusion effect) which accumulate or propagate in the solution.

APPENDIX D

STARTING APPROXIMATION

To obtain the flow-field properties along the initial left-running characteristic, ray 1-3 in sketch (a), properties are first calculated at the end-wall points 0 and 1. Properties at point 0, shown as the origin of the xt diagram, are obtained from the standard shock-jump relations for shock-wave reflection at a plane, nonconducting wall. As is appropriate for the instant of reflection, $\alpha = 0$ behind the reflected shock wave. Properties at the second point, point 1, can be approximated in a number of ways. However, it is desirable to have a good approximation so as to minimize the perturbation introduced into the resulting solution. Since the velocity on the end wall vanishes and heat-transfer effects are ignored, it is reasonable to assume that the enthalpy along the end wall is a constant for a short time – that is, $h_1 = h_0$. The degree of dissociation at point 1 can then be found in terms of the temperature from

$$\alpha_1 = \frac{h_0 - (7/2)RT_1 - e_{v_1}}{(3/2)RT_1 - e_{v_1} + D} \quad (D1)$$

where

$$e_{v_1} = \frac{R\theta_v}{e^{\theta_v/T_1} - 1} \quad (D2)$$

is the vibrational energy at point 1. The temperature has been used as the independent variable, primarily for convenience, and is evaluated at point 1 using

$$T_1 = T_0 - \Delta T \quad (D3)$$

where ΔT is a specified initial perturbation. The third property required to define the nonequilibrium state at point 1 is obtained by assuming, consistent with the constant-enthalpy approximation, that $P_1 = P_0$.

The time duration of the starting approximation Δt , defined as

$$\Delta t = t_1 - t_0 = \frac{2\alpha_1}{(d\alpha/dt)_1 + (d\alpha/dt)_0} \quad (D4)$$

is, of course, required to be very small in comparison with the total time scale of the relaxation process. Thus, the assumptions of constant enthalpy and pressure during this interval should not seriously affect the resultant solution. The starting-time interval is controlled by the magnitude of the initial temperature perturbation ΔT . The magnitude of ΔT for each case was selected to yield an optimum mesh spacing, by a trial-and-error procedure, for the resulting solution. Although the initial gradients of flow-field variables are somewhat insensitive to ΔT , the solution can become unstable at large times if ΔT is chosen too large. On the other hand, if ΔT is too small, excessive

computer time will be required to obtain a solution. A compromise for the cases considered here put ΔT in the range $10^\circ < \Delta T < 400^\circ$ K.

The remaining points shown along ray 1-3 are obtained by first calculating the properties at point 3 using the procedure for shock-wave points described in appendix C. The position of point 3 is located by the intersection of the reflected shock wave from point 0, slope $dx/dt = -V_0$ and the left-running characteristic from point 1, slope $dx/dt = -a_1$. Linear interpolation between points 1 and 3 is used to obtain the properties at the intermediate point 2. The ray 1-3 is now ready for use as a known ray for the subsequent flow-field calculations.

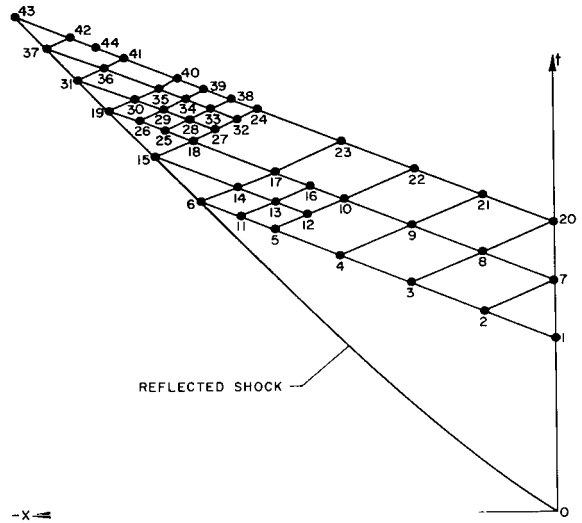
APPENDIX E

FINE-MESH SCHEME AND ROLLBACK TECHNIQUE

To maintain sufficient accuracy and stability in the region immediately behind the reflected shock wave, where very large gradients are present in the thermodynamic properties, a fine mesh is incorporated into this region of the network. The number of points within this fine mesh is dependent on the magnitude of the temperature gradient adjacent to the reflected shock wave.

Sketch (b) is a diagram of the points involved in a typical, narrow segment of the fine-mesh network. For clarity, left-running characteristics calculated prior to ray 1-6 are not shown; this discussion concerns the logic of the fine-mesh network that follows after points 1-6 are known. The points are labeled in the order that they are calculated.

The calculation technique for obtaining the position and properties of points 7 through 10 is described in appendix C. The next step is to select the number of points to be added to the basic network. In the present study, one new point is added along the line segment between the shock-wave point and the preceding point (between points 6 and 5) for each 400° K of temperature difference. For example, if the temperature difference between points 6 and 5 is less than 400° K, a single new point is added, as shown by point 11 in sketch (b). If the temperature difference is between 400° and 800° K, then two new points (equally spaced) are added; for example, see points 25 and 26 along the next continuous left-running characteristic in the sketch.



Sketch (b).—Fine-mesh characteristic network.

The properties P , u , T , and α at point 11 are found by interpolating between the known property values at points 4, 5, and 6 (using a quadratic fit for the property values as a function of distance along the characteristic). Other needed properties are calculated directly from these interpolated property values. The number of points added (always equally spaced) along the ray from point 5 to 10 is the same as added between points 5 and 6 — in this case, one. The properties P and u at that point, labeled 12, are established by linear interpolation. Other properties are computed with the standard interior-point technique involving streamline integration and linear interpolation between points 4 and 5.

On the basis of the known properties at points 5, 6, 11, and 12, the location and properties at points 13 and 14 follow directly from the standard interior-point routine. Point 15 is then established using the conventional shock-point routine. The auxiliary ray 12-15 now enables

calculation of points 16 through 19 (using standard routines) with an improved accuracy over that attainable without the auxiliary ray.

The calculation of ray 20-43 is intended to represent the case where the temperature difference between points 19 and 18 is between 400° and 800° K. The order of the calculations is self explanatory. The techniques are the same as described above for the case of a single added point adjacent to the shock wave. In this case, however, an additional point, point 44, is added midway between points 41 and 42 (by interpolation) to maintain more uniform mesh spacing in the next calculated characteristic. In fact, to maintain uniform spacing, only points 21-24, 40, 44, and 43 are used during calculation of the subsequent complete left-running ray.

It should be noted that, in addition to the calculations described here, each of the points in the fine-mesh part of the network is iterated once using the technique discussed in appendix C.

Since each new continuous left-running characteristic involves one more computing point than the previous ray, it is obvious that the number of computing points can rapidly become unmanageable from the viewpoints of computer storage, time to achieve a solution, and printout-statement volume. To keep the number of calculations to a reasonable level, a rollback technique is employed. In short, each time a ray reaches 175 points, the ray is redivided into 150 equally spaced points with the properties at each new point determined by linear interpolation.

REFERENCES

1. Johnson, Charles D.; and Britton, D.: Shock Waves in Chemical Kinetics: The Use of Reflected Shock Waves. J. Chem. Phys., vol. 38, no. 7, April 1, 1963, pp. 1455-1462.
2. Kamimoto, G.; Akamatsu, T.; and Hasegawa, T.: Effect of Shock Attenuation on Reflected Shock Waves. CP2, Oct. 1962, Dept. Aerospace Engr., Kyoto Univ., Japan.
3. Rudinger, George: Effect of Boundary-Layer Growth in a Shock Tube on Shock Reflexion from a Closed End. Phys. Fluids, vol. 4, no. 12, Dec. 1961, pp. 1463-1473.
4. Mark, Herman: The Interaction of a Reflected Shock Wave with the Boundary Layer in a Shock Tube. NACA TM 1418, 1958.
5. Strehlow, R. A.; and Cohen, A.: Limitation of the Reflected Shock Technique for Studying Fast Chemical Reactions and its Application to the Observation of Relaxation in Nitrogen and Oxygen. J. Chem. Phys., vol. 30, no. 1, Jan. 1959, pp. 257-265.
6. Lin, Shoa-Chi, and Fyfe, Walter I.: Low-Density Shock Tube for Chemical Kinetics Studies. Phys. Fluids, vol. 4, no. 2, Feb. 1961, pp. 238-249.
7. Sturtevant, Bradford; and Slachmuylders, Erik: End Wall Heat-Transfer Effects on the Trajectory of a Reflected Shock Wave: Phys. Fluids, vol. 7, no. 8, Aug. 1964, pp. 1201-1207.
8. Goldsworthy, F. A.: The Structure of a Contact Region, with Application to the Reflexion of a Shock from a Heat Conducting Wall. J. Fluid Mech., vol. 5, pt. 1, Jan. 1959, pp. 164-176.
9. Hanson, Ronald K.: Shock-Wave Reflection in a Relaxing Gas. J. Fluid Mech., vol. 45, pt. 4, 1971, pp. 721-746.
10. Baganoff, D.: Experiments on the Wall-Pressure History in Shock-Reflexion Processes. J. Fluid Mech., vol. 23, pt. 2, 1965, pp. 209-228.
11. Johannesen, N. H.; Bird, G. A.; and Zienkiewicz, H. K.: Theoretical and Experimental Investigations of the Reflexion of Normal Shock Waves with Vibrational Relaxation. J. Fluid Mech., vol. 30, pt. 1, 1967, p. 51.
12. Hanson, Ronald K.: Chemical Relaxation Behind Strong Shock Waves in Diatomic Gases. M. S. Thesis, Arizona State Univ., Tempe, Arizona, June, 1965.
13. Greene, Edward F.; and Toennies, J. P.: *Chemical Reactions in Shock Waves*. Academic Press, N.Y., 1964.
14. Ferri, Antonio, ed.: *Fundamental Data Obtained From Shock Tube Experiments*. Pergamon Press, N.Y., 1961.
15. Chu, Boa-Teh: Wave Propagation and the Method of Characteristics in Reacting Gas Mixtures with Applications to Hypersonic Flow. TN 57-213, May 1957, Wright Air Development Center, Wright-Patterson Air Force Base, Ohio.
16. Vincenti, Walter G.; and Kruger, Charles H., Jr.: *Introduction to Physical Gasdynamics*. John Wiley & Sons., Inc., N.Y., 1965.

17. Presley, Leroy L.; and Hanson, Ronald K.: Numerical Solutions of Reflected Shock-Wave Flowfields with Nonequilibrium Chemical Reactions. *AIAA J.*, vol. 7, no. 12, Dec. 1969, pp. 2267-2273.
18. Capiaux, R. and Washington, M.: Nonequilibrium Flow Past a Wedge. *AIAA J.*, vol. 1, no. 3, March 1963, pp. 650-660.

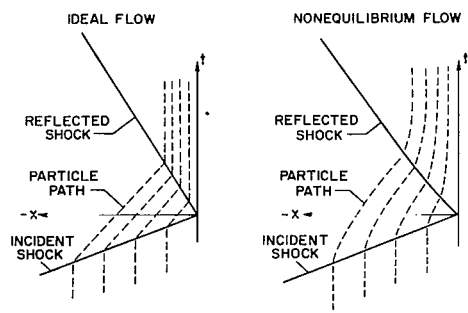


Figure 1.— Comparison of reflected-shock wave $x-t$ diagram for ideal and nonequilibrium flow.

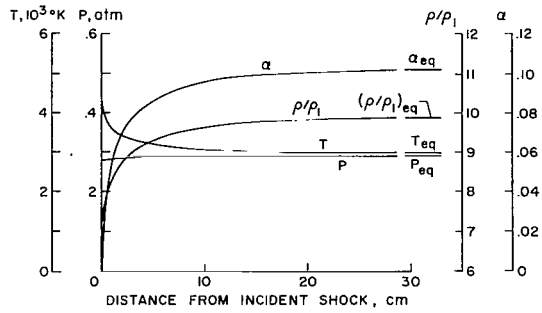


Figure 3.— Incident-shock flow-field profiles for case 1.

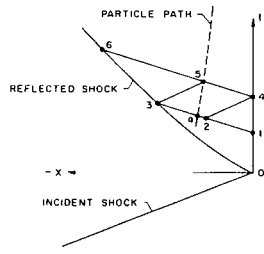


Figure 2.— Characteristic network construction.

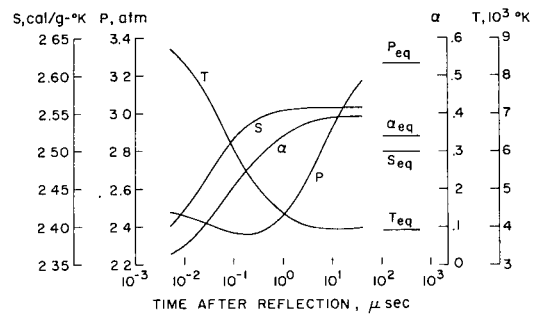


Figure 4.— End-wall properties as a function of time after reflection, case 1.

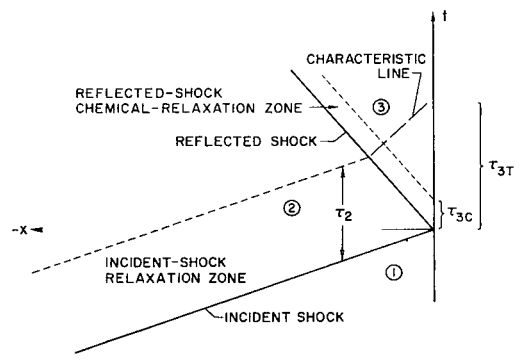
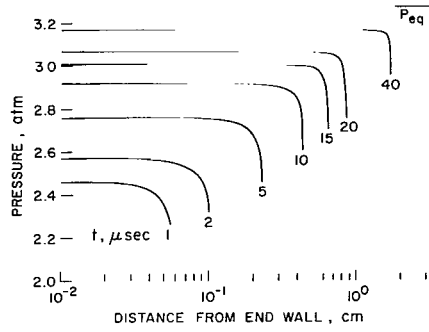
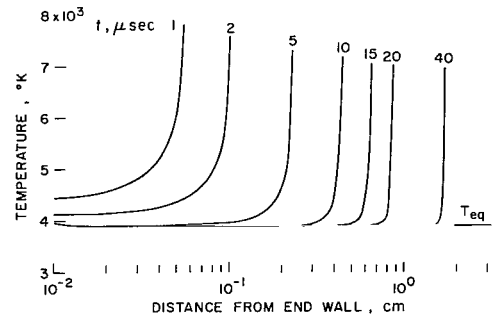


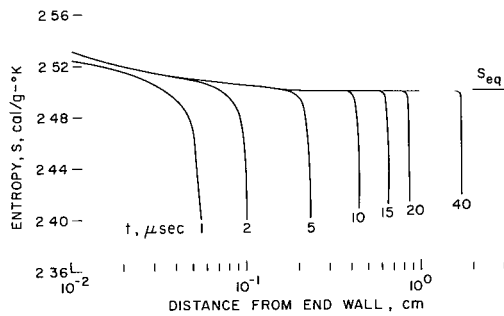
Figure 5.— Graphic description of controlling times for reflected-shock-wave relaxation.



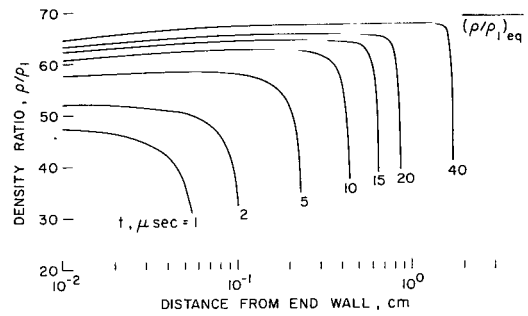
(a) Pressure.



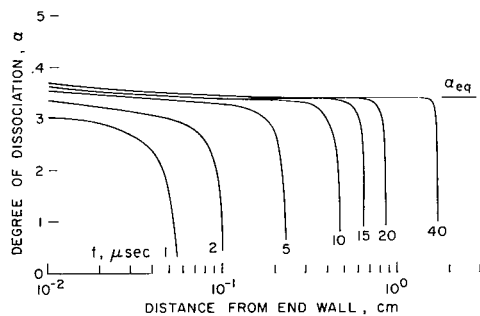
(d) Temperature.



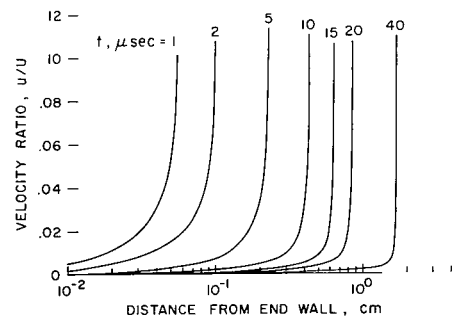
(b) Entropy.



(e) Density.



(c) Degree of dissociation.



(f) Flow velocity relative to end wall.

Figure 6.— Flow-field properties as a function of distance from the end wall for discrete times after reflection, case 1

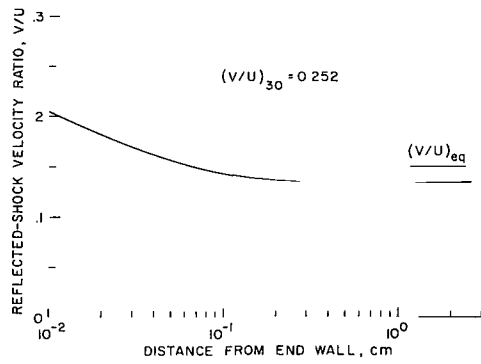


Figure 7.— Reflected-shock velocity relative to end wall, case 1.

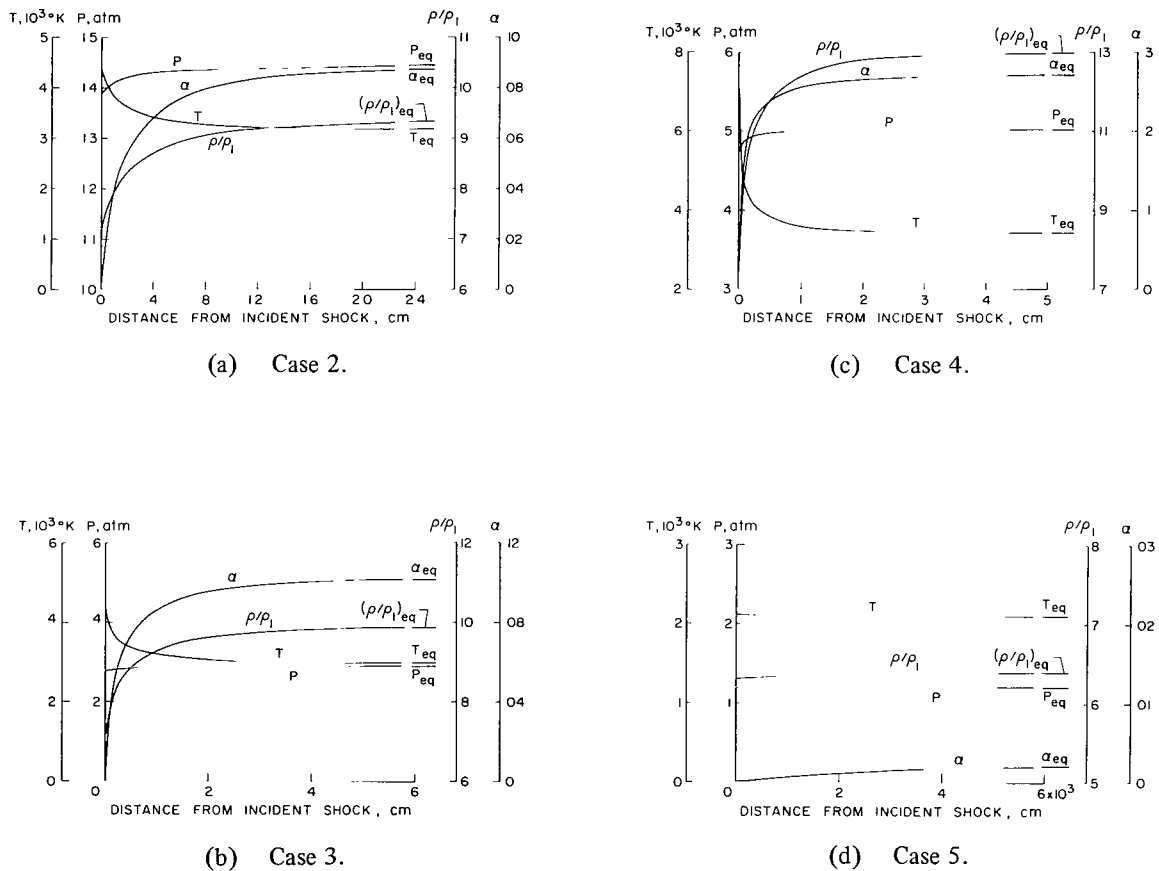
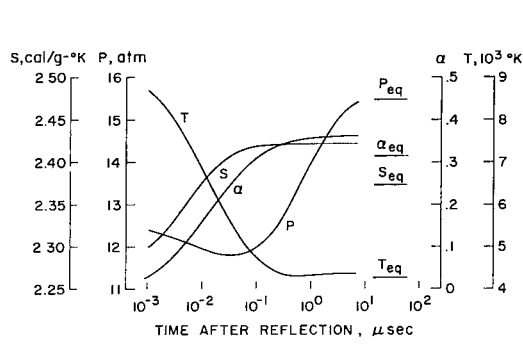
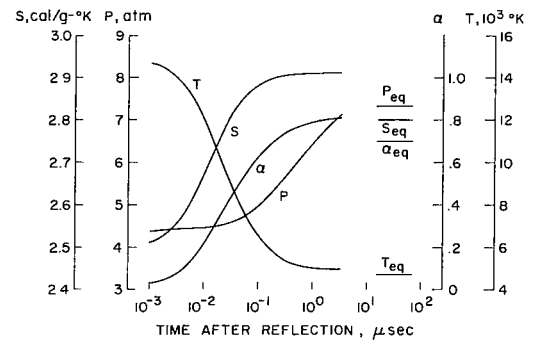


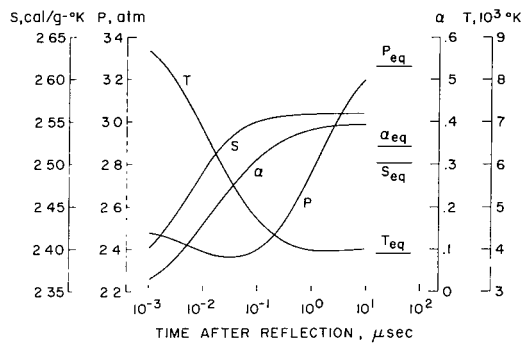
Figure 8.— Comparison of incident-shock flow fields, cases 2-5.



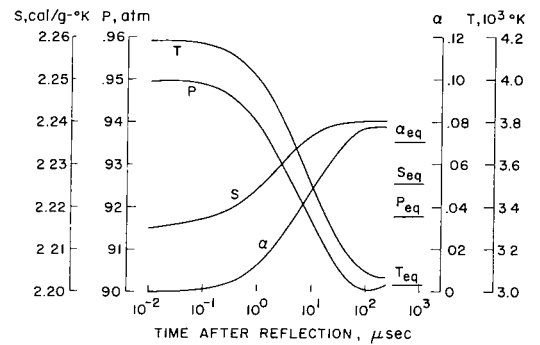
(a) Case 2.



(c) Case 4.



(b) Case 3.



(d) Case 5.

Figure 9.— Comparison of end-wall properties as a function of time after reflection, cases 2-5.

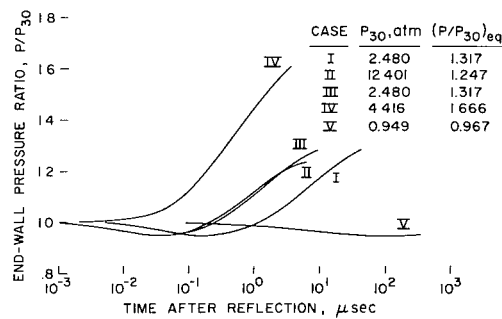
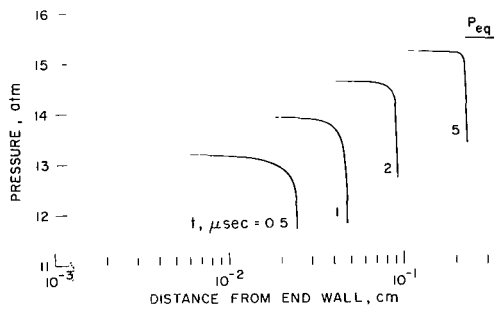
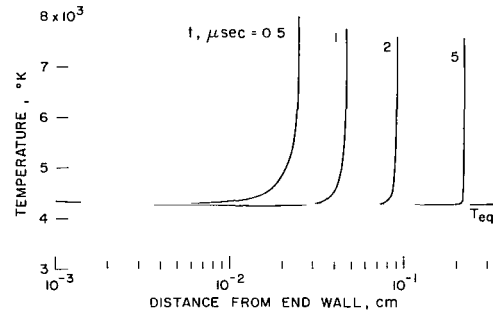


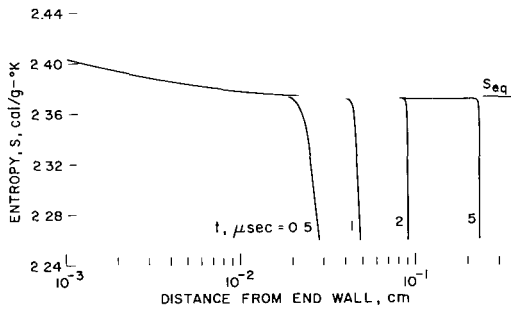
Figure 10.— Comparison of end-wall pressure histories, cases 1-5.



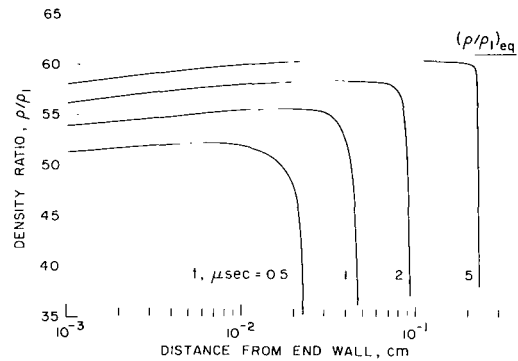
(a)



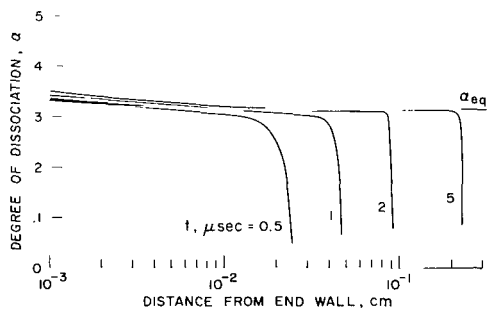
(d)



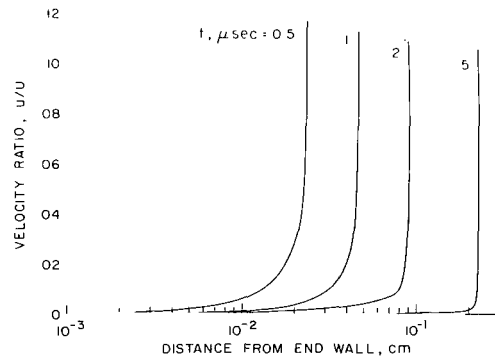
(b)



(e)

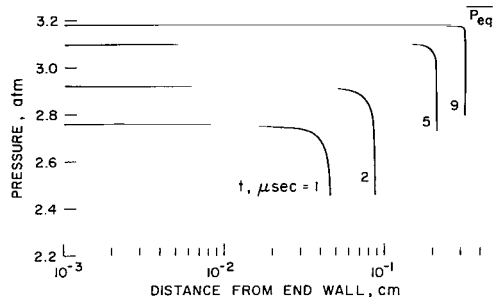


(c)

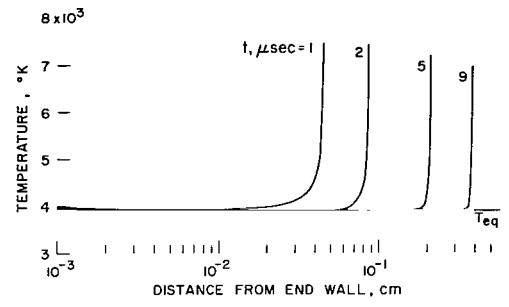


(f)

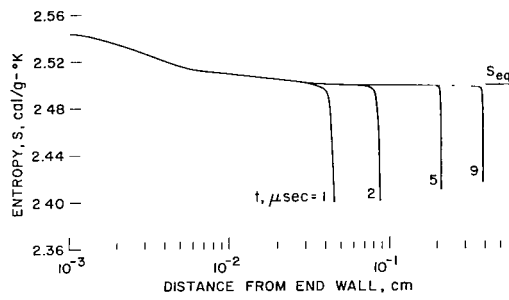
Figure 11.— Flow-field properties as a function of distance from the end wall for discrete times after reflection, case 2.



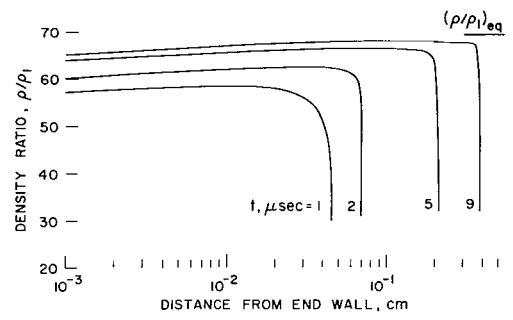
(a)



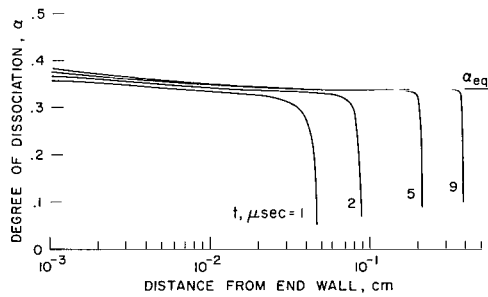
(d)



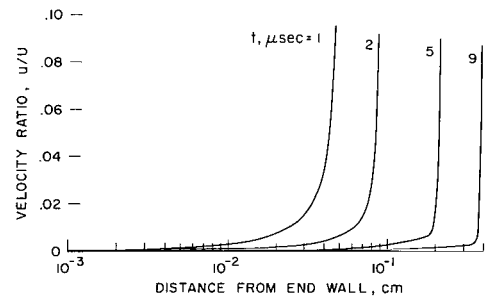
(b)



(e)

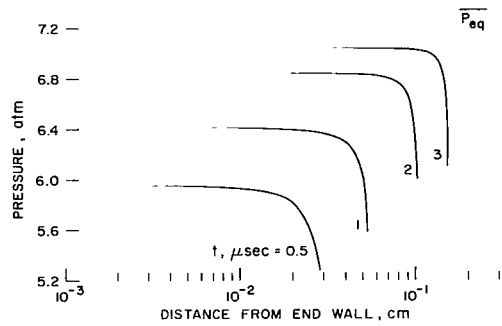


(c)

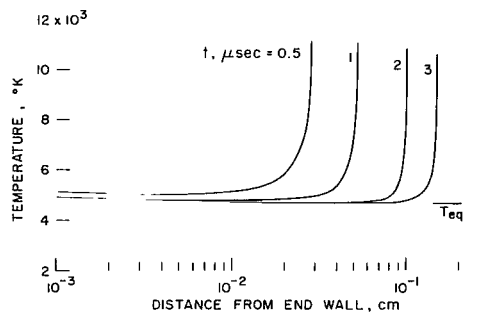


(f)

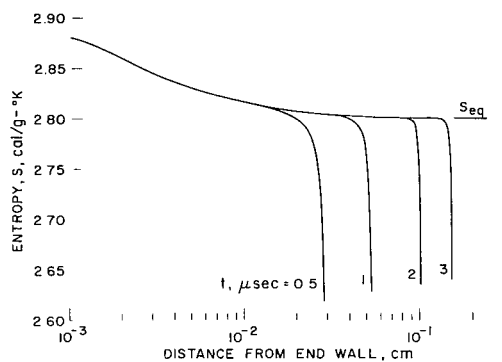
Figure 12.— Flow-field properties as a function of distance from the end wall for discrete times after reflection, case 3.



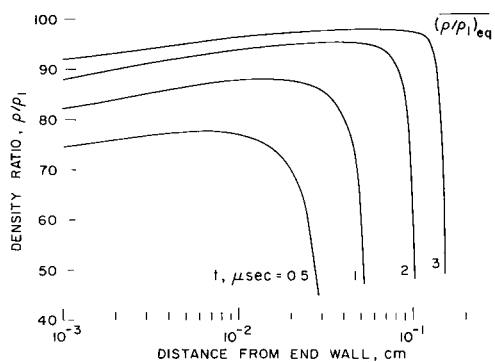
(a)



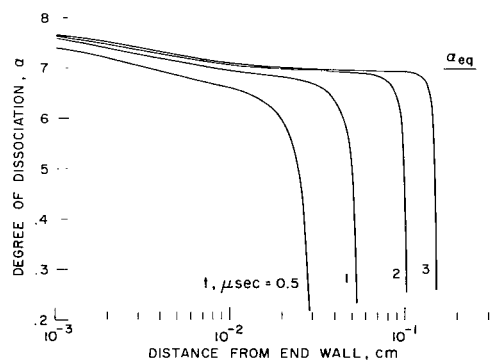
(d)



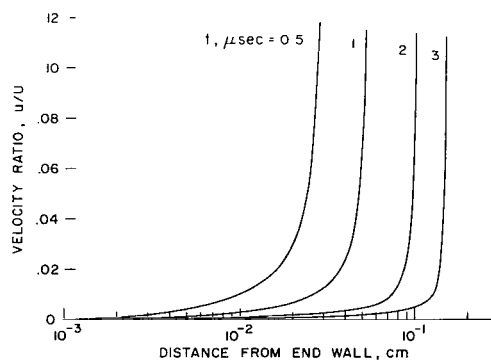
(b)



(e)

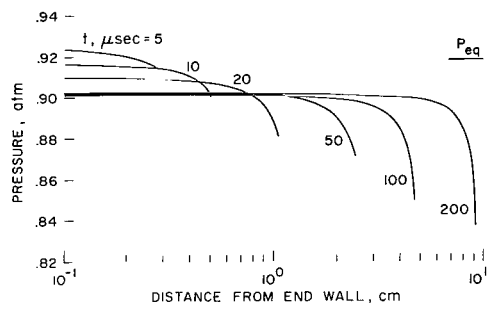


(c)

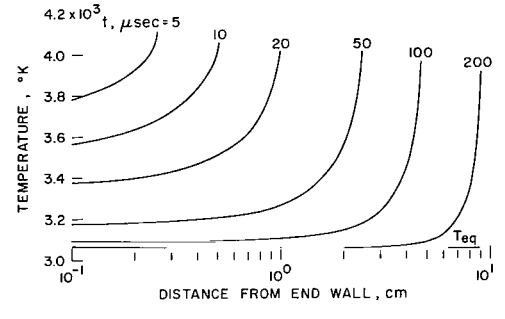


(f)

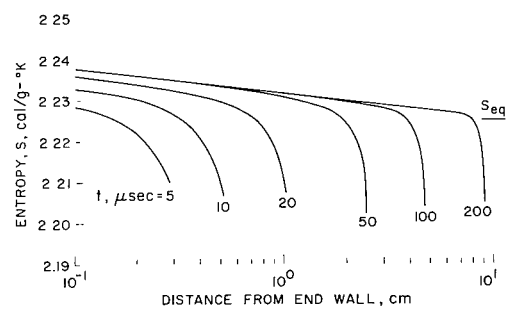
Figure 13.— Flow-field properties as a function of distance from the end wall for discrete times after reflection, case 4.



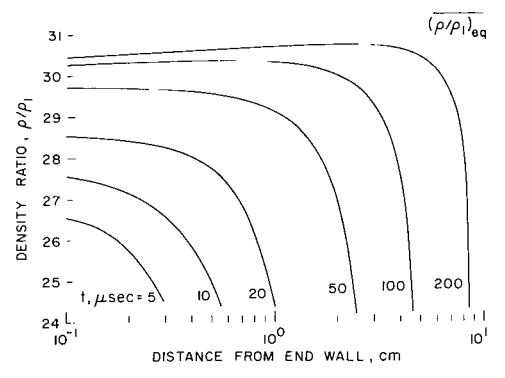
(a)



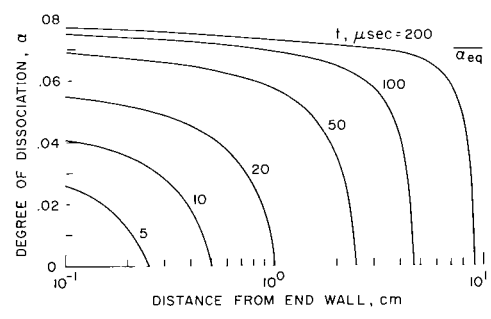
(d)



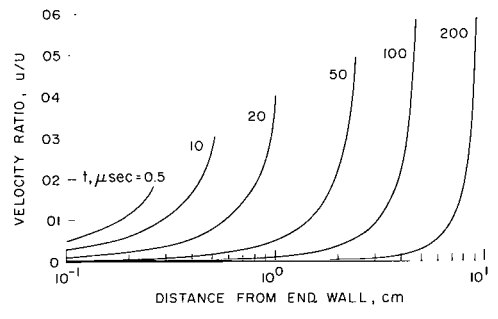
(b)



(e)

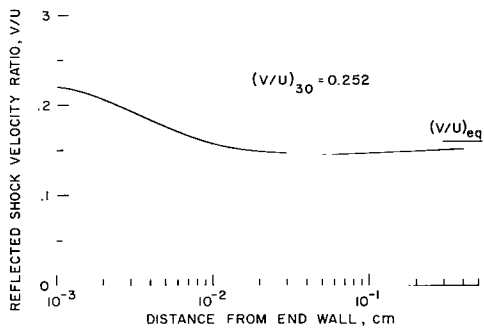


(c)

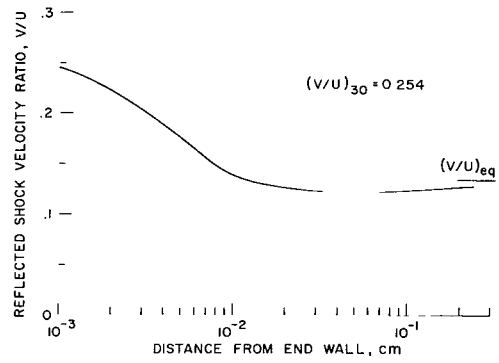


(f)

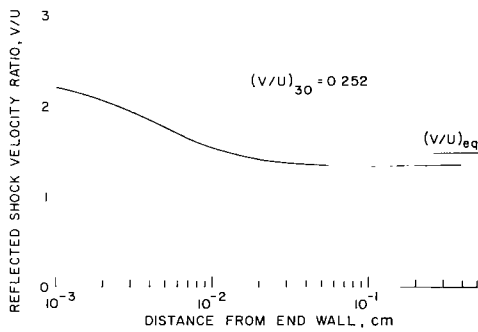
Figure 14.— Flow-field properties as a function of distance from the end wall for discrete times after reflection, case 5.



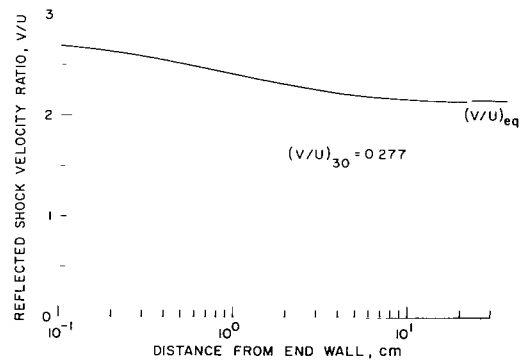
(a) Case 2.



(c) Case 4.



(b) Case 3.



(d) Case 5.

Figure 15.— Comparison of reflected-shock velocities, cases 2-5.

OFFICIAL BUSINESS
PENALTY FOR PRIVATE USE \$300

FIRST CLASS MAIL

POSTAGE AND FEES PAID
NATIONAL AERONAUTICS AND
SPACE ADMINISTRATION



NASA 451

003 001 C1 U 12 720728 SC0903DS
DEPT OF THE AIR FORCE
AF WEAPONS LAB (AFSC)
TECHNICAL LIBRARY/DOUL/
ATTN: E LOU BOWMAN, CHIEF
KIRTLAND AFB NM 87117

POSTMASTER: If Undeliverable (Section 158
Postal Manual) Do Not Return

"The aeronautical and space activities of the United States shall be conducted so as to contribute . . . to the expansion of human knowledge of phenomena in the atmosphere and space. The Administration shall provide for the widest practicable and appropriate dissemination of information concerning its activities and the results thereof."

— NATIONAL AERONAUTICS AND SPACE ACT OF 1958

NASA SCIENTIFIC AND TECHNICAL PUBLICATIONS

TECHNICAL REPORTS: Scientific and technical information considered important, complete, and a lasting contribution to existing knowledge.

TECHNICAL NOTES: Information less broad in scope but nevertheless of importance as a contribution to existing knowledge.

TECHNICAL MEMORANDUMS: Information receiving limited distribution because of preliminary data, security classification, or other reasons.

CONTRACTOR REPORTS: Scientific and technical information generated under a NASA contract or grant and considered an important contribution to existing knowledge.

TECHNICAL TRANSLATIONS: Information published in a foreign language considered to merit NASA distribution in English.

SPECIAL PUBLICATIONS: Information derived from or of value to NASA activities. Publications include conference proceedings, monographs, data compilations, handbooks, sourcebooks, and special bibliographies.

TECHNOLOGY UTILIZATION PUBLICATIONS: Information on technology used by NASA that may be of particular interest in commercial and other non-aerospace applications. Publications include Tech Briefs, Technology Utilization Reports and Technology Surveys.

Details on the availability of these publications may be obtained from:

SCIENTIFIC AND TECHNICAL INFORMATION OFFICE

NATIONAL AERONAUTICS AND SPACE ADMINISTRATION

Washington, D.C. 20546